The Astrophysical Journal, 922:190 (23pp), 2021 December 1 https://doi.org/10.3847/1538-4357/ac1cdb

Particle Reacceleration by Turbulence and Radio Constraints on Multimessenger High-energy Emission from the Coma Cluster

Kosuke Nishiwaki[1], Katsuaki Asano[1], and Kohta Murase[2,3,4,5]
[1] Institute for Cosmic Ray Research, The University of Tokyo, 5-1-5 Kashiwanoha, Kashiwa, Chiba 277-8582, Japan
[2] Department of Physics, The Pennsylvania State University, University Park, PA 16802, USA
[3] Department of Astronomy & Astrophysics, The Pennsylvania State University, University Park, PA 16802, USA
[4] Center for Multimessenger Astrophysics, Institute for Gravitation and the Cosmos, The Pennsylvania State University, University Park, PA 16802, USA
[5] Yukawa Institute for Theoretical Physics, Kyoto University, Kyoto 606-8502, Japan
Received 2021 May 6; revised 2021 August 5; accepted 2021 August 10; published 2021 November 30

Abstract

Galaxy clusters are considered to be gigantic reservoirs of cosmic rays (CRs). Some of the clusters are found with extended radio emission, which provides evidence for the existence of magnetic fields and CR electrons in the intra-cluster medium. The mechanism of radio halo (RH) emission is still under debate, and it has been believed that turbulent reacceleration plays an important role. In this paper, we study the reacceleration of CR protons and electrons in detail by numerically solving the Fokker–Planck equation, and show how radio and gamma-ray observations can be used to constrain CR distributions and resulting high-energy emission for the Coma cluster. We take into account the radial diffusion of CRs and follow the time evolution of their one-dimensional distribution, by which we investigate the radial profile of the CR injection that is consistent with the observed RH surface brightness. We find that the required injection profile is nontrivial, depending on whether CR electrons have a primary or secondary origin. Although the secondary CR electron scenario predicts larger gamma-ray and neutrino fluxes, it is in tension with the observed RH spectrum for hard injection indexes, $\alpha < 2.45$. This tension is relaxed if the turbulent diffusion of CRs is much less efficient than the fiducial model, or the reacceleration is more efficient for lower-energy CRs. In both the secondary and primary scenario, we find that galaxy clusters can make a sizable contribution to the all-sky neutrino intensity if the CR energy spectrum is nearly flat.

Unified Astronomy Thesaurus concepts: Galaxy clusters (584)

1. Introduction

The detection of the cosmic background radiation of high-energy neutrinos by the IceCube neutrino observatory is an observational milestone of high-energy astrophysics (Aartsen et al. 2013; IceCube Collaboration 2013). The observed intensities around $\sim$100 TeV to $\sim$1 PeV are consistent with the Waxman −Bahcall bound (Waxman & Bahcall 1999), which may indicate that high-energy neutrinos and ultra-high-energy cosmic rays (UHECRs) come from the same source class (Yoshida & Murase 2020). The majority of IceCube neutrinos are still unknown, but such neutrinos should be produced by hadronic interactions such as pp or $p\gamma$ collisions of relativistic protons. Many candidate sources have been proposed, including starburst galaxies (e.g., Loeb & Waxman 2006; Murase et al. 2013; Tamborra et al. 2014; Senno et al. 2015) and galaxy clusters (e.g., Berezinsky et al. 1997; Murase et al. 2008; Kotera et al. 2009; Murase et al. 2013; Zandanel et al. 2015; Fang & Olinto 2016; Hussain et al. 2021).

Galaxy clusters are the latest and largest cosmological structure in the universe. A fraction of the gravitational energy dissipated during structure formation can be expended on accelerating cosmic rays via shocks and turbulence (e.g., Ensslin et al. 1998; Fujita et al. 2003; Brunetti & Lazarian 2007). Galaxy clusters are regarded as "cosmic-ray reservoirs" (e.g., Murase et al. 2013; Bykov et al. 2019) since they can confine cosmic-ray ions for up to a cosmological time with their large volumes and turbulent magnetic fields. Cosmic-ray protons (CRPs) accumulated in the intra-cluster medium (ICM) undergo inelastic pp collisions with thermal protons, which produce charged and neutral pions. Secondary particles including gamma-ray photons, neutrinos, and cosmic-ray electrons/positrons (CREs) are produced as decay products of those pions.

Radio observations have detected diffuse synchrotron emission from many clusters. Some are in the form of giant radio haloes (RHs), roundish emission extended over the X-ray emitting regions, and some others are radio relics, elongated emission often found in peripheral regions (see van Weeren et al. 2019 for an observational review). The large extension of those radio structures is a major challenge for theoretical modeling, because the cooling time of radio-emitting CREs is far shorter than the time required to diffuse across the emission region. That naturally requires in-situ injection or acceleration of CREs at the emission region (see Brunetti & Jones 2014 for a theoretical review). There are two possibilities for the origin of CREs in the ICM. One is the secondary origin, in which CREs are born as secondaries produced via inelastic pp collisions (e.g., Dennison 1980; Blasi & Colafrancesco 1999; Kushnir & Waxman 2009). The other is the primary origin, i.e., CREs are injected from the same sources as CRPs. The former scenario naturally explains the extension of RHs, since parent CRPs can diffuse over the halo volume until they collide with thermal protons.

The physical origin of primary CRs is still an open question, but the fact that diffuse radio emission is usually found in merging systems suggests the possible connection between structure formation and CR acceleration (e.g., Govoni et al. 2001; Venturi et al. 2007; Cassano et al. 2010; Kale et al. 2013). The shock waves formed through the merger of clusters and mass accretion could accelerate CRs through the first-order Fermi acceleration process (e.g., Kang et al. 2012; Ryu et al. 2019). Internal sources such as ordinary galaxies, galaxy

mergers, and active galactic nuclei (AGNs) are also considered to be the sources of CRs (e.g., Berezinsky et al. 1997; Enßlin et al. 1997; Kashiyama & Meszaros 2014; Yuan et al. 2018). In the accretion/merger shock scenario, the contribution from massive clusters at low redshifts is expected to be dominant, while in the internal accelerator scenario the contribution from low-mass clusters including high-redshift ones is important (Murase & Waxman 2016; Fang & Murase 2018).

The most plausible origin of RHs is the reacceleration of seed CREs. In the so-called turbulent reacceleration scenario, stochastic interactions between CREs and turbulence caused by the merger of clusters accelerate seed CREs up to ∼GeV energies. The interactions between particles and waves that transfer energies from the turbulence to particles in the ICM have been studied in detail (e.g., Yan & Lazarian 2002; Brunetti & Lazarian 2007). Alfvénic turbulence exhibits the anisotropic cascade that makes the interaction between particles inefficient at smaller scales (Goldreich & Sridhar 1995; Yan & Lazarian 2002), so a resonant interaction called transit-time damping (TTD) with isotropic fast modes is often considered to be the mechanism of the reacceleration (e.g., Brunetti & Lazarian 2011; Teraki & Asano 2019).

This scenario can reproduce various observational features of RHs. For example, it predicts that the lifetime of RHs is about ∼100 Myr, which can explain the bimodality in the radio–X-ray luminosity relation (Cassano & Brunetti 2005; Cuciti et al. 2015). This timescale may correspond to the turbulence surviving timescale after the cluster merger. That can also explain the apparent break feature appearing in the spectrum of the Coma RH (e.g., Pizzo 2010; Brunetti et al. 2013) as the balance between radiative cooling and the reacceleration of the CREs with energies around ∼GeV.

It is also notable that gamma-ray observations by the Fermi satellite with its Large Area Telescope (LAT) give stringent constraints on the density of CRPs in the Coma cluster (e.g., Ackermann et al. 2016a). Xi et al. (2018) reported the first detection of an extended gamma-ray source in the direction of the Coma with an analysis of Fermi data. More recently, the existence of a gamma-ray source, 4FGL J1256.9+2736, is indicated in the updated 4GFL catalog (Abdollahi et al. 2020; Ballet et al. 2020). Adam et al. (2021) also found a significant signal and discussed the CRP content in the ICM and its possible connection to the radio emission.

A number of theoretical works have discussed the origin of CREs in the Coma cluster (e.g., Schlickeiser et al. 1987; Giovannini et al. 1993; Blasi & Colafrancesco 1999; Ohno et al. 2002; Kushnir & Waxman 2009; Zandanel et al. 2014; Brunetti et al. 2017; Pinzke et al. 2017). The ratio between primary and secondary CREs in the seed population for reacceleration was discussed in, e.g., Brunetti et al. (2017), Pinzke et al. (2017), and Adam et al. (2021), but it is largely uncertain because of the parameter degeneracy in the reacceleration process. The diffusion of parent CRPs from primary accelerators has been of interest (e.g., Keshet 2010; Keshet & Loeb 2010), and has also been separately investigated in the calculation of high-energy emission or escaping CRs (e.g., Kotera et al. 2009; Fang & Olinto 2016; Fang & Murase 2018; Hussain et al. 2021).

In this paper, we evaluate multiwavelength radiation from the radio to gamma-rays and the neutrino emission from the Coma cluster. We follow the time evolution of the CR distribution in the Coma cluster from the radio-quiet state to the radio-loud state. Concerning primary CRs, we present two extreme cases. One is the "secondary-dominant model," where all CREs are injected as secondary products of *pp* collisions. The other is the "primary-dominant model," where most of CREs in the ICM are injected from the same source as primary CRPs. We also test two types of turbulent reacceleration: "hard-sphere" and "Kolmogorov" type.

This paper is organized as follows. In Section 2 we introduce the basic formalism for the CR acceleration and evolution, and in Section 3 we explain the procedure to put constraints on model parameters from the observational properties of the Coma RH and summarize resulting fluxes including cosmic rays, gamma-rays, and neutrinos. In Section 4, we evaluate the intensity of the background emission and compare our results with earlier studies. Our main results are summarized in Section 5. Throughout this paper, we adopt the ΛCDM model with $H_0 = 100\ \ h\,\mathrm{km\,s^{-1}\,Mpc^{-1}}$, $h = 0.7$, $\Omega_m = 0.28$, and $\Omega_\Lambda = 0.72$.

2. Cosmic-Ray Distribution and Evolution in the ICM

In our calculation, the Coma cluster is considered to be a spherical gas cloud containing CRs. We first show the basic equations that describe the time evolution of the CR distribution in Section 2.1. The physical processes considered here are radiative and collisional cooling (Section 2.1), hadronic interactions to generate pions and secondary CRE injection from their decay (Section 2.2), and the spatial diffusion and acceleration due to the interaction with turbulence (Section 2.4). The injection spectrum of the primary CRs is assumed to be a single power-law spectrum with a cutoff (Section 2.3). The procedure to obtain observable quantities such as flux and surface brightness from the CR distribution functions is explained in Section 2.5. The initial condition is explained in Section 2.6. Finally, we summarize our model parameters in Section 2.7.

2.1. Basic Equations

We assume spherical symmetry and define the distribution function of CRs in radial position r, momentum p, and time t as $N_s^{\rm tot}(r, p, t)$ (where the index s denotes particle species), which is related to the total particle number through $N_s^{\rm tot}(t) = \int dr \int dp N_s(r, p, t)$. The number density of the particle, $n_s(r, t)$, is then $n_s(r, t) = \int dp N_s(r, p, t)/(4\pi r^2)$.

To follow the time evolution of $N_s(r, p, t)$, we solve the isotropic one-dimensional Fokker–Planck (FP) equation. For protons, it takes the form

$$\frac{\partial N_{\rm p}}{\partial t} = \frac{\partial}{\partial p}\left[N_{\rm p}\left(b_{\rm C}^{(p)} - \frac{1}{p^2}\frac{\partial}{\partial p}(p^2 D_{pp})\right)\right] + \frac{\partial^2}{\partial p^2}[D_{pp} N_{\rm p}] + \frac{\partial}{\partial r}\left[D_{rr}\frac{\partial N_{\rm p}}{\partial r} - \frac{2}{r} N_{\rm p} D_{rr}\right] + Q_{\rm p}(r, p) - \frac{N_{\rm p}}{\tau_{pp}(r, p)}, \quad (1)$$

where $b_{\rm C}^{(p)}$ represents the momentum loss rate ($b \equiv -dp/dt$) due to the Coulomb collisions (Equation (2)), D_{rr} and D_{pp} are the spatial and momentum diffusion coefficients due to interactions with turbulence (Equations (21) and (24)), and $Q_{\rm p}(r, p)$ denotes the injection of primary CRPs (Equation (18)).

The number of primary CRPs injected per unit volume per unit time per momentum interval can be expressed as $q_{\rm p}(r, p) = Q_{\rm p}(r, p)/(4\pi r^2)$. The value τ_{pp} denotes the pp collision timescale (Equation (9)). For simplicity, we ignore the effect of repeated collisions of a CRP, so we do not follow an energy loss per collision. The cooling due to the pp collision is expressed similar to escape as $-N_{\rm p}/\tau_{pp}$ in the FP equation. This term is smaller than other terms in Equation (1) and has only a negligible effect in the evolution of the CRP spectrum, so we do not include the inelasticity coefficient $\kappa_{pp} \approx 0.5$ in Equation (1). This means that we neglect multiple pp collisions experienced by a single CRP.

The momentum loss of a CRP due to the combined effect of CRP-p, CRP-e Coulomb interactions can be expressed as (Petrosian & Kang 2015)

$$b_{\rm C}^{(p)}(r, p) = \frac{3}{2}(\sigma_{\rm T} n_{\rm th} c) m_{\rm e} c \frac{\ln\Lambda}{\beta_{\rm p}^2}\left(1 - \frac{k_{\rm B}T/2}{E_{\rm p} - m_{\rm p}c^2}\right) \times \sum_{s=e,p} \frac{m_{\rm e}}{m_s}\left[{\rm Erf}(\sqrt{x_s}) - \frac{2}{\sqrt{\pi}}\sqrt{x_s}e^{-x_s}\right], \simeq 3.5 \times 10^{-29} {\rm erg\ cm^{-1}} \frac{1}{\beta_{\rm p}^2}\left(\frac{n_{\rm th}}{1{\rm cm^{-3}}}\right)\left(\frac{\ln\Lambda}{38}\right) \times \left[1 - \frac{k_{\rm B}T/(2m_{\rm p}c^2)}{\sqrt{1 + (p/(m_{\rm p}c))^2} - 1}\right] \times \sum_{s=e,p} \frac{m_{\rm e}}{m_s}\left(\int_0^{\sqrt{x_s}} dy e^{-y^2} - \sqrt{x_s}e^{-x_s}\right), \quad (2)$$

where $\sigma_{\rm T}$ is the Thomson cross section, Λ is the Coulomb logarithm, $x_s \equiv \frac{(E_{\rm p} - m_{\rm p}c^2)}{k_B T}\frac{m_s}{m_{\rm p}}$, where the index $s = {\rm e}, {\rm p}$ stands for the species of the target particles, $E_{\rm p} = \sqrt{m_{\rm p}^2 c^4 + p^2 c^2}$, and $\beta_{\rm p}$ is the particle velocity in unit of c. The function ${\rm Erf}(x)$ in Equation (2) stands for the error function, and $n_{\rm th}$ and T are the density and temperature of the thermal gas in ICM, respectively.

In this paper, we adopt the beta-model profile for the thermal electron density derived from X-ray observations (Briel et al. 1992):

$$n_{\rm th}(r) = n_{\rm th}(0)\left\{1 + \left(\frac{r}{r_{\rm c}}\right)^2\right\}^{-\frac{3}{2}\beta}, \quad (3)$$

where $n_{\rm th}(0) = 3.42 \times 10^{-3}\ {\rm cm^{-3}}$, $\beta = 0.75$, and the core radius of the Coma cluster is given by $r_c = 290$ kpc.

We also use the temperature profile following (Bonamente et al. 2009; Pinzke et al. 2017)

$$k_{\rm B}T(r) = 8.25{\rm keV}\left[1 + \left(\frac{2r}{r_{200}}\right)^2\right]^{-0.32}, \quad (4)$$

where the virial radius of the Coma cluster is $r_{200} = 2.3$ Mpc (Reiprich & Bohringer 2002). Assuming that the turbulence responsible for the reacceleration is driven by a cluster merger, the terms proportional to D_{pp} have finite values only after the merger (Sections 3.2, 2.6).

For electrons and positrons, the FP equation becomes

$$\frac{\partial N_{\rm e}}{\partial t} = \frac{\partial}{\partial p}\left[N_{\rm e}\left(b_{\rm rad} + b_{\rm C}^{(e)} - \frac{1}{p^2}\frac{\partial}{\partial p}(p^2 D_{pp})\right)\right] + \frac{\partial^2}{\partial p^2}[D_{pp}N_{\rm e}] + \frac{\partial}{\partial r}\left[D_{rr}\frac{\partial N_{\rm e}}{\partial r} - \frac{2}{r}N_{\rm e}D_{rr}\right] + Q_{\rm e}(r, p; N_{\rm p}). \quad (5)$$

The energy loss rate of a CRE due to CRE-e collisions[6] in the ICM is

$$b_{\rm C}^{(e)}(r, p) = \frac{3}{2}(\sigma_{\rm T} c n_{\rm th}) m_{\rm e} c \frac{1}{\beta_{\rm e}^2} B_{\rm rel}, \quad (6)$$

$$\simeq 3.05 \times 10^{-29}\ {\rm erg\ cm^{-1}} \frac{1}{\beta_{\rm e}^2}\left(\frac{n_{\rm th}}{1\ {\rm cm^{-3}}}\right) \times \left[1 + \frac{1}{74.8}\ln\left(\frac{p/m_{\rm e}c}{(n_{\rm th}/1\ {\rm cm^{-3}})}\right)\right], \quad (7)$$

where $\beta_{\rm e}$ is the velocity of the CRE and $B_{\rm rel}$ is the dimensionless stopping number (see Gould 1972, Equation (5.5)).

The radiative momentum loss term, $b_{\rm rad}$, includes both synchrotron radiation and inverse-Compton scattering (ICS); $b_{\rm rad} = b_{\rm syn} + b_{\rm IC}$. The bremsstrahlung loss is negligible compared to $b_{\rm C}^{(e)} + b_{\rm rad}$ (Sarazin 1999). Radio-emitting CREs in the ICM also emit $\sim$10 keV photons due to the ICS with cosmic microwave background (CMB) photons. We use the formulae given in Rybicki & Lightman (1985) and Inoue & Takahara (1996) for these processes (see Equation (A5) for the ICS radiation).

The injection of CREs can be divided into primary and secondary injections; $Q_{\rm e}(r, p; N_{\rm p}) = Q_{\rm e}^{\rm sec}(r, p; N_{\rm p}) + Q_{\rm e}^{\rm pri}(r, p)$; (see Equations (11) and (19)).

2.2. Production of Secondary Electrons

Inelastic collisions between CRPs and thermal protons in the ICM lead to mesons that are primarily pions ($p + p \rightarrow \pi^{0,\pm} + X$), whose decay channels are

$$\begin{cases} \pi^0 \rightarrow 2\gamma, \ \pi^{\pm} \rightarrow \mu^{\pm} + \nu_{\mu}(\bar{\nu}_{\mu}), \\ \mu^{\pm} \rightarrow e^{\pm} + \bar{\nu}_{\mu}(\nu_{\mu}) + \nu_{\rm e}(\bar{\nu}_{\rm e}). \end{cases} \quad (8)$$

The collision timescale is written as

$$\tau_{pp}(r, p) = \frac{1}{c n_{\rm th}(r)\sigma_{\rm inel}(p)}, \quad (9)$$

where $\sigma_{\rm inel}(p) \approx 34$ mb is the total inelastic cross section, which is given in, e.g., Kamae et al. (2006). Here, we assume that the ICM is pure hydrogen plasma and use Equation (3) for the density of thermal protons, although the existence of helium nuclei can affect the pp production rate in the ICM.[7] Using the inclusive cross section for charged and neutral pion production $\sigma^{0,\pm}$, it can be written as $\sigma_{\rm inel}(p) = \sigma^0(p) + \sigma^{\pm}(p)$.

[6] The loss due to CRE-p collisions is negligible since the lightest particle contributes most to the stopping power of the plasma (e.g., Dermer & Menon 2009).

[7] As discussed in Adam et al. (2020), the production rate of secondary particles would be increased by a factor of $\sim$1.5, considering the helium mass fraction of 0.27.

The injection rate of generated pions $Q_\pi(E_\pi)$; (which has the same dimension as Q_p and Q_e in Equations (1) and (5)) can be calculated from

$$Q_\pi^{0,\pm}(E_\pi; N_p) = n_{th}(r)c\int_{E_{th}}^{\infty} dp\beta_p N_p(r, p, t) \times \sigma^{0,\pm}(p)\frac{F_\pi(E_\pi, E_p)}{E_p}, \quad (10)$$

where $E_{th} \approx 1.22$ GeV is the threshold energy for the pion production, and $F_\pi(E_\pi, E_p)$ is the spectrum of pions produced in a single pp collision by a CRP of energy E_p. The injection rate of pions per unit volume, $q_\pi^{0,\pm}$, is expressed as $q_\pi^{0,\pm} = Q_\pi^{0,\pm}/(4\pi r^2)$. We adopt the approximate expression of $F_\pi(E_\pi, E_p)$ given in Kelner et al. (2006; see Equation (B1) in the Appendix) for both neutral and charged pions. To distinguish the cross sections for neutral and charged pion productions, we adopt the inclusive cross section, $\sigma^{0,\pm}(p)$, given in Kamae et al. (2006, 2007). There is a slight ($\lesssim$50%) difference in the pion production rate around 100 MeV between our method and, for example, that of Brunetti et al. (2017), where the isobaric model by Stecker (1970) and high-energy model by Kelner et al. (2006) are adopted at lower and higher energies, respectively. The uncertainty in the secondary production rate, including that arising from the helium abundance noted above, is much less significant than the uncertainty in the CR injection rate or the turbulent reacceleration in our modeling (Section 3).

Using the injection rate of pions Q_π, the injection rate of secondary electrons/positrons can be written as (e.g., Brunetti et al. 2017)

$$Q_e^{sec}(r, p; N_p) = \int dE_\pi \int dE_\mu Q_\pi(E_\pi; N_p) \times F_e(E_e, E_\mu, E_{\pi^\pm})F_\mu(E_\mu, E_{\pi^\pm}), \quad (11)$$

where $F_\mu(E_\mu, E_{\pi^\pm})$ is the spectrum of muons from the decay of $\pi^\pm$ with energy E_π, which can be obtained with simple kinematics. Hereafter in this section, we omit the $\pm$ symbol on $\pi^\pm$. In the rest frame of a pion, the energy of secondary muons and muonic neutrinos are $E_\mu' = \frac{m_\pi^2c^4 + m_\mu^2c^4}{2m_\pi c^2} \approx 110$ GeV, $E'_{\nu_\mu} = \frac{m_\pi^2c^4 - m_\mu^2c^4}{2m_\pi c^2} \approx 29.9$ GeV, where we neglect the mass of neutrinos. The Lorentz factor and velocity of the muons are then $\gamma_\mu' = (m_\pi^2 + m_\mu^2)/(2m_\pi m_\mu) \simeq 1.039$ and $\beta_\mu' \simeq 0.2714$ (e.g., Moskalenko & Strong 1998). Since a pion decays isotropically in its rest frame, the spectrum in the source frame is

$$F_\mu(E_\mu, E_\pi) = \frac{m_\pi^2}{m_\pi^2 - m_\mu^2}\frac{1}{\sqrt{E_\pi^2 - m_\pi^2c^4}}, \quad (12)$$

within the energy range $\gamma_\mu^- m_\mu c^2 \leqslant E_\mu \leqslant \gamma_\mu^+ m_\mu c^2$, where $\gamma_\mu^\pm = \gamma_\pi\gamma_\mu'(1 \pm \beta_\pi\beta_\mu')$ are the minimum and maximum Lorentz factors of the muon in the laboratory system, respectively. The function $F_e(E_e, E_\mu, E_\pi)$ stands for the spectrum of secondary electrons and positrons from decay of the muon of energy E_μ, which also depends on the energy of the parent pion of E_π since the muons from $\pi^\pm \rightarrow \mu^\pm + \nu_\mu(\bar{\nu}_\mu)$ are fully polarized. The expression is given by (e.g., Gaisser 1991; Blasi & Colafrancesco 1999):

$$F_e(E_e, E_\mu, E_\pi) = \frac{4}{\beta_\mu E_\mu}\left[\frac{5}{12} - \frac{3}{4}\lambda^2 + \frac{1}{3}\lambda^3 - \frac{P_\mu(E_\pi, E_\mu)}{2\beta_\mu}\left\{\frac{1}{6} - \left(\beta_\mu + \frac{1}{2}\right)\lambda^2 + \left(\beta_\mu + \frac{1}{3}\right)\lambda^3\right\}\right], \quad \text{for}\left(\frac{1-\beta_\mu}{1+\beta_\mu} \leqslant \lambda \leqslant 1\right), \quad (13)$$

and

$$F_e(E_e, E_\mu, E_\pi) = \frac{4}{\beta_\mu E_\mu} \times \left[\frac{\lambda^2\beta_\mu}{(1-\beta_\mu)^2}\left\{3 - \frac{2}{3}\lambda\left(\frac{3+\beta_\mu^2}{1-\beta_\mu}\right)\right\} - \frac{P_\mu(E_\pi, E_\mu)}{1-\beta_\mu}\left\{\lambda^2(1+\beta_\mu) - \frac{2\lambda^2}{1-\beta_\mu}\left[\frac{1}{2} + \lambda(1+\beta_\mu)\right] + \frac{2\lambda^3(3+\beta_\mu^2)}{3(1-\beta_\mu)^2}\right\}\right], \quad \text{for}\left(0 \leqslant \lambda \leqslant \frac{1-\beta_\mu}{1+\beta_\mu}\right), \quad (14)$$

where

$$\lambda = \frac{E_e}{E_\mu},\ \beta_\mu = \sqrt{1 - \frac{m_\mu^2c^4}{E_\mu^2}}, \quad (15)$$

and

$$P_\mu(E_\pi, E_\mu) = \frac{1}{\beta_\mu}\left[\frac{2E_\pi\xi}{E_\mu(1-\xi)} - \frac{1+\xi}{1-\xi}\right], \quad \xi = \frac{m_\mu^2}{m_\pi^2}. \quad (16)$$

Following Brunetti & Blasi (2005), we assume that the muon spectrum is approximated by the delta function at the energy $E_\mu = \frac{1}{2}(E_\mu^{min} + E_\mu^{max})$ in the laboratory system, that is,

$$F_\mu(E_\mu, E_\pi) = \delta\left(E_\mu - \frac{m_\pi^2 - m_\mu^2}{m_\pi^2}\frac{E_\pi}{2\beta_\mu'}\right). \quad (17)$$

In this case, the integral with respect to E_μ in Equation (11) can be performed self-evidently. The resulting injection spectrum of secondary CREs has a power-law index of $\alpha_e = \alpha + \Delta$ with $\Delta \sim 0.05-0.1$ for $N_p \propto p^{-\alpha}$ for parent CRPs (e.g., Kamae et al. 2006; Kelner et al. 2006).

2.3. Injection of Primary Cosmic Rays

Galaxy clusters can be regarded as reservoirs of CRs because they can confine accelerated particles for a cosmological timescale (Murase & Beacom 2013). The candidate CR accelerators include structure formation shocks, cluster mergers, AGNs, ordinary galaxies, and galaxy mergers.

Among these, structure formation shocks should have a connection with the occurrence of RHs because they are usually found in merging systems (e.g., Cassano et al. 2010). During a merger between two clusters with the same mass and radius of $M \sim 10^{15}\ M_{\odot}$ and $R \sim 2$ Mpc, respectively, the gravitational energy of $E \sim GM^2/R \sim 10^{64}$ erg dissipates within the dynamical timescale of $t_{\rm dyn} \sim 10^9$ yr. Assuming that $\sim$1% of the energy is used to accelerate CRs, the injection power of primary CRs is evaluated as $L_{\rm CR} \sim 10^{45}\ {\rm erg\ s^{-1}}$.

In a simple test particle regime, the diffusive shock acceleration theory predicts the CR injection with a single power-law distribution in momentum, whose slope depends only on the shock Mach number. We assume that primary CRPs are injected with a single power-law spectrum with an exponential cutoff:

$$Q_{\rm p}(r, p) = C_{\rm p}^{\rm inj} p^{-\alpha} \exp\left[-\frac{E_{\rm p}}{E_{\rm p}^{\rm max}}\right] K(r), \tag{18}$$

where $E_{\rm p}^{\rm max}$ stands for the maximum energy of primary CRPs. We adopt $E_{\rm p}^{\rm max} = 100$ PeV as a reference value, though the energy up to the ankle ($\sim 10^{18.5}$ eV) could be achieved by primary sources, such as AGNs (e.g., Kotera et al. 2009; Fang & Murase 2018) or strong shocks (Kang et al. 1997; Inoue et al. 2005, 2007). The Larmor radius of CRPs with $E_{\rm p}^{\rm max} = 100$ PeV in a μG magnetic field is $r_{\rm L} \sim 100$ pc, which is much smaller than the typical scale of the accretion shocks, $\sim$Mpc. The minimum momentum of CRPs is taken to be $p = 30\ {\rm MeV/c}$, which is about ten times larger than the momentum of the thermal protons.

The function $K(r)$ represents the radial dependence of the injection, which is to be determined to reproduce the observed surface brightness profile of the RH (Section 3.2). Note that the luminosity of the injection, i.e., the normalization $C_{\rm p}^{\rm inj}$, is tuned to match the observed radio synchrotron flux at 350 MHz (Section 3.2).

A certain amount of electrons should also be injected as primary CRs. The presence of primary CREs affects the relative strength of hadronic emission to leptonic ones. However, the ratio of primary to secondary CREs is usually uncertain in observations. We treat the primary CRE injection by introducing a parameter $f_{\rm ep}$:

$$Q_{\rm e}^{\rm pri}(r, p) = f_{\rm ep}\, Q_{\rm p}(r, p). \tag{19}$$

Using this relation, we extrapolate Equation (18), which is valid only above the minimum momentum of the CRP, $p = 30\ {\rm MeV\ c^{-1}}$, to the minimum momentum of CREs, $p_{\rm e} = 0.3 m_{\rm e} c = 150\ {\rm KeV\ c^{-1}}$. The contribution of CREs below this energy is negligible due to the strong Coulomb cooling compared to the acceleration (Figure 1 left). Concerning $f_{\rm ep}$, we consider two example cases: the secondary-dominant model ($f_{\rm ep} = 0$) and the primary-dominant model ($f_{\rm ep} = 0.01$). The possible radial dependence of $f_{\rm ep}$ (e.g., Pfrommer et al. 2008) is not considered in our calculation.

The former case, $f_{\rm ep} = 0$, is motivated by the injection from AGNs (e.g., Fang & Murase 2018), where only high-energy ions can diffuse out from their radio lobes, while CREs lose their energies inside the lobes due energy losses during the expansion. Another possibility for that case is that CRs are accelerated at shock waves in the ICM with low Mach numbers (e.g., Ha et al. 2020), where particles with smaller rigidities ($= pc/(Ze)$) are less likely to recross the shock front, and therefore the acceleration of electrons from thermal energies can be more inefficient compared to that for protons (Brunetti & Jones 2014).

That said, $f_{\rm ep} = 0.01$ corresponds to the observed CRE to CRP ratio in our Galaxy (e.g., Schlickeiser 2002). If CRs in the ICM are provided by the internal sources, that value may be the upper limit for $f_{\rm ep}$. Some numerical studies suggest that the fluctuations at the shock vicinity, such as electrostatic or whistler waves, support the injection of CREs into the Fermi acceleration process (e.g., Amano & Hoshino 2008; Riquelme & Spitkovsky 2011), which could potentially increase the CRE to CRP ratio. However, the injection processes of CREs at weak shocks in a high-beta plasma are still under debate (e.g., Kang et al. 2019).

2.4. Particle Acceleration and Diffusion in the ICM

The magnetic field in the Coma cluster is well studied with rotation measure (RM) measurements. Here, we use the following scaling of the magnetic field strength with cluster thermal density:

$$B(r) = B_0 \left(\frac{n_{\rm th}(r)}{n_{\rm th}(0)}\right)^{\eta_B}, \tag{20}$$

where $B_0 = 4.7\ \mu$G and $\eta_B = 0.5$ are the best-fit values for the RM data (Bonafede et al. 2010). The uncertainty in the magnetic field estimate and its impact on our results are discussed in Section 4.1.

CRs in the ICM undergo acceleration and diffusion due to the interaction with MHD turbulences. We assume that the spatial diffusion is caused by the isotropic pitch angle scattering with Alfvén waves. When the Larmor radius of a particle $r_{\rm L}$ is smaller than the maximum size of the turbulent eddy, $l_{\rm c}^{\rm A} \sim 0.1$ Mpc, the propagation of the particle is in the diffusive regime. The diffusion coefficient in that regime can be written as (e.g., Murase et al. 2013; Fang & Olinto 2016)

$$D_{rr}(r, p) = \frac{1}{3}\left(\frac{B(r)}{\delta B}\right)^2 \beta_{\rm p} c r_{\rm L}^{1/3} (l_{\rm c}^{\rm A})^{2/3}. \tag{21}$$

For reference, the typical value of D_{rr} in our Galaxy is $D_{rr} \sim$ a few $\times\ 10^{28}\ {\rm cm^2\ s^{-1}}$ for protons with 1 GeV (e.g., Strong et al. 2007), which should be smaller than Equation (21) due to the shorter coherent length in our Galaxy. We take $\delta B \sim B$ at $l_{\rm c}^{\rm A} = 0.1$ Mpc and the Kolmogorov scaling for Alfvénic turbulence, neglecting the possible r dependence of these quantities for simplicity. Then, the spatial diffusion coefficient is written as

$$D_{rr}(r, p) \simeq 6.8 \times 10^{29}\ {\rm cm^2 s^{-1}} \beta_{\rm p} \left(\frac{l_{\rm c}^{\rm A}}{0.1\ {\rm Mpc}}\right)^{2/3} \times \left(\frac{p}{1\ {\rm GeV/c}}\right)^{1/3} \left(\frac{B(r)}{1\ \mu G}\right)^{-1/3}. \tag{22}$$

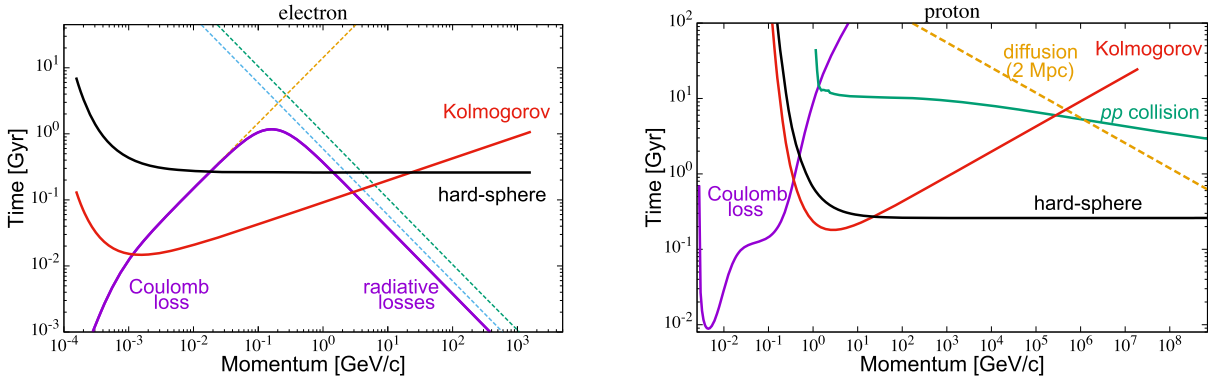

Figure 1. Left: physical timescales of CREs at $r = 50$ kpc from the center of the cluster as functions of the momentum. The black line corresponds to hard-sphere type acceleration with $\tau_{\rm acc} = 260$ Myr, while the red line corresponds to the Kolmogorov type with $\tau_{\rm acc} = 100$ Myr. The acceleration timescale becomes comparable to the cooling timescale of CREs around $E_{\rm e} \sim 1$ GeV (see the main text for details). Dashed lines show the cooling timescale of the Coulomb collision (orange), synchrotron radiation (cyan), and ICS (green). The total cooling timescale is shown with a solid magenta line. Right: physical timescales of CRPs. The dashed orange line and the green line show the diffusion timescale on a 2 Mpc scale and the *pp* collision timescale with $n_{\rm th} = n_0$, respectively.

A similar value has often been used (e.g., Murase et al. 2008), although larger values may also be possible (Keshet 2010).

The time required to diffuse a distance comparable to the value of the radial position of the particle r can be estimated as

$$t_{\rm diff}(r, p) = \frac{r^2}{4D_{rr}(r, p)} \propto p^{-1/3}. \tag{23}$$

The diffusion timescale for GeV electrons over the scale of RHs ($r \sim 1$ Mpc) is much longer than the Hubble time. This requires that CREs are injected in situ in the emitting region. Moreover, $t_{\rm diff}$ for parent CRPs can also be ∼Gyr, so the resulting spatial distribution of GeV electrons depends on the injection profile. Note that CRPs with $r_{\rm L}$ larger than $l_{\rm c}^{\rm A}$ are in the semi-diffusive regime, where $t_{\rm diff} \propto p^{-2}$.

We simply write the momentum diffusion coefficient as a power-law function of particle momentum with an exponential cutoff:

$$D_{pp}(r, p) = \frac{p^2}{(q+2)\tau_{\rm acc}} \left(\frac{p}{1\ {\rm GeV/c}}\right)^{q-2} \times \exp\left[-\frac{E_{\rm p}}{E_c^{\rm max}(r)}\right] \exp\left(-\frac{m_s c}{p}\right), \tag{24}$$

where the exponential cutoffs at both the maximum energy $E_c^{\rm max}$ and the minimum momentum $m_{\rm sc}$ are introduced, where the index s denotes the particle species. For simplicity, we adopt $E_{\rm c}^{\rm max}(r) = qB(r)l_{\rm c}^{\rm F} \sim 9 \times 10^{19}(B(r)/1\ \mu G)(l_{\rm c}^{\rm F}/0.1\ {\rm Mpc})$ eV for the maximum energy of CRs achieved by that acceleration; that is, the particles whose Larmor radius larger than $l_{\rm c}^{\rm F}$ cannot be accelerated efficiently, where $l_{\rm c}^{\rm F}$ is the maximum size of the turbulent eddy of compressible turbulence. We assume $l_{\rm c}^{\rm F} = 0.1$ Mpc as a reference, and this is somewhat lower than the Hillas limit with the system size (∼Mpc). Khatri & Gaspari (2016) measured the power spectrum of the pressure fluctuation in Coma using the observation of the thermal Sunyaev–Zel'dovich effect (SZ), and found an injection scale of ∼0.5 Mpc. Considering the uncertainty in the measured scale, which is basically an interpolation between the SZ analysis and the X-ray analysis by Churazov et al. (2012), our assumption of $l_{\rm c}^{\rm F} = 0.1$ Mpc is compatible with those observations. Our calculation is not sensitive to $E_{\rm c}^{\rm max}$, since the maximum energy of CRPs hardly reaches such high energies starting from $E_{\rm p}^{\rm max} = 100$ PeV of Equation (18); (see also Section 3.5).

The index q is treated as a model parameter (Section 2.7). We examine two cases for q: $q = 2$ and $5/3$. We call $q = 2$ "hard-sphere type" acceleration and $q = 5/3$ "Kolmogorov-type" acceleration. The parameter $\tau_{\rm acc}$ denotes the acceleration timescale of particles with momentum $p = 1$ GeV/c, which is constrained from the spectral shape of the RH (Section 3.2). Note that we assume $\tau_{\rm acc}$ is constant with the radius for simplicity.

The acceleration time of CRs is estimated as

$$t_{\rm acc}(r, p) = \frac{p^2}{(2+q)D_{pp}(r, p)} \propto p^{2-q}. \tag{25}$$

This timescale is independent of p in the hard-sphere case ($q = 2$), while it is shorter for the smaller momentum in the Kolmogorov case ($q = 5/3$). The momentum diffusion coefficient for stochastic acceleration by pitch angle scattering with Alfvénic waves takes the form $D_{pp} \propto p^w$ (i.e., $q = w$), where the index w has the same value as the slope of the turbulent spectrum: $w = \frac{5}{3}$ for the Kolmogorov scaling and $w = \frac{3}{2}$ for the Iroshnikov–Kraichnan (IK) scaling (e.g., Becker et al. 2006). Brunetti & Lazarian (2007) self-consistently calculated D_{pp} for TTD with a compressive MHD mode via quasi-linear theory (QLT). In this case, the acceleration timescale (Equation (25)) for CR particles does not depend on particle momentum, because all CRs are assumed to interact with the turbulence at the cutoff scale. Thus, this mechanism has the same index q as our hard-sphere model, $q = 2$.

Assuming the IK scaling for the compressible turbulence, $\tau_{\rm acc}$ for the TTD acceleration can be estimated as (e.g., Brunetti 2015)

$$\tau_{\rm acc} \approx \frac{4c\rho}{\pi} I_\theta^{-1}(x) \left[\int_{k_L}^{k_{\rm cut}} dk k W(k)\right]^{-1} \simeq 300{\rm Myr} \left(\frac{L}{300{\rm kpc}}\right)\left(\frac{\mathcal{M}_{\rm s}}{0.5}\right)^{-4}\left(\frac{c_{\rm s}}{10^8{\rm cm/s}}\right)^{-1}, \tag{26}$$

where ρ is the mass density of the ICM, $W(k)$ is the total energy spectrum of the compressible turbulence,

$I_\theta(x) \equiv \int_0^{\arccos(x)} d\theta \frac{\sin^3\theta}{|\cos\theta|}\left[1-\left(\frac{x}{\cos\theta}\right)^2\right]$ with $x = c_s/c$, c_s is the sound speed of the ICM, $k_L \equiv 2\pi/L$ and $k_{\rm cut}$ are wavenumbers corresponding to the injection scale and the cutoff scale, respectively, and $\mathcal{M}_s$ is the Mach number of the turbulent velocity at the injection scale. Here, the cutoff scale of the turbulence is determined by the dissipation due to the TTD interaction with thermal electrons (see Brunetti & Lazarian 2007).

Figure 1 shows physical timescales of various terms in Equations (1) and (5). Note again that we assume $\tau_{\rm acc}$ to be constant with radius. Following Brunetti et al. (2017), we choose $\tau_{\rm acc} \sim 300$ Myr, which is a typical value to explain the break in the spectrum around 1.4 GHz (see Section 3.2). We do not solve the decay of turbulence, so $\tau_{\rm acc}$ remains a constant for several 100 Myr.

Radio surveys have revealed that clusters with similar X-ray luminosities can be divided into two populations: "radio-loud" clusters hosting RHs and "radio-quiet" clusters that do not show any sign of cluster-scale radio emission. According to the Extended Giant Metrewave Radio Telescope (GMRT) Radio Halo Survey (EGRHS), the fraction of radio-loud clusters is about 30% (Kale et al. 2013). Moreover, intermediate clusters between these two states are hardly detected. This clear bimodality implies the existence of a mechanism that quickly turns the RH on and off. The timescale for clusters staying in the intermediate state, $\tau_{\rm in}$, can be estimated as the time between the formation and observation of clusters times the fraction of clusters in that region: $\tau_{\rm in} \sim 100$ Myr (Brunetti et al. 2009). Considering that RHs tend to be found in merging systems, the turbulence generated during cluster mergers could rapidly accelerate CRs within a few $\times 100$ Myr (Brunetti & Jones 2014). The damping of MHD waves might play a role in turning off RHs, as it enables super-Alfvénic streaming of CRPs (Wiener et al. 2013). In our calculation, we first prepare an initial distribution of CRs that corresponds to the radio-quiet state as explained in Section 2.6, and then turn on the reacceleration and follow the evolution of the CR spectra.

2.5. Emissivities and Radiative Transfer

In this section, we describe how to calculate the fluxes of electromagnetic waves and neutrinos from the given N_p and N_e. We here identify two types of radiation: *leptonic* radiation is synchrotron radiation and the one from ICS with CMB photons, while *hadronic* ones are associated with the decay of pions produced by the *pp* collision. The emissivity is defined as the energy emitted per frequency interval per unit volume per unit time per unit solid angle. The emissivity of the ICS radiation is shown in the Appendix (see Equation (A4)). The emissivity of the hadronic gamma-rays is calculated with the π^0 injection spectrum q_π^0 (the number of pions injected per logarithmic energy per unit volume per unit time):

$$\varepsilon_\gamma(E_\gamma) = 2E_\gamma \int_{E_{\rm min}(E_\gamma)} \frac{q_\pi^0(E_\pi)}{\sqrt{E_\pi^2 - m_\pi^2 c^4}} dE_\pi, \tag{27}$$

where $E_{\rm min}(E_\gamma) = E_\gamma + (m_\pi^2 c^4)/(4E_\gamma)$ and $q_\pi^{0,\pm} = Q_\pi^{0,\pm}/(4\pi r^2)$. The gamma-ray photons produced by the decay of π^0 of energy E_π are distributed in the energy range of $\frac{1}{2}E_\pi(1-\beta_\pi) \leqslant E_\gamma \leqslant \frac{1}{2}E_\pi(1+\beta_\pi)$ with an equal probability.

Muonic neutrinos are produced from the decay of both charged pions and secondary muons. Using the injection spectrum of charged pions, $q_\pi^\pm$, the emissivity is written as

$$\begin{aligned}\varepsilon_{\nu_\mu}(E_{\nu_\mu}) &= 2E_{\nu_\mu}\int_0^1 (f_{\nu_\mu^{(1)}}(x) + f_{\nu_\mu^{(2)}}(x)) q_\pi^\pm(E_\pi)\frac{dx}{x}, \\ &= E_{\nu_\mu}\left[\frac{1}{\zeta}\int_0^\zeta q_\pi^\pm\left(\frac{E_{\nu_\mu}}{x}\right)\frac{dx}{x}\right. \\ &\quad \left. + \int_0^1 f_{\nu_\mu^{(2)}}(x) q_\pi^\pm\left(\frac{E_{\nu_\mu}}{x}\right)\frac{dx}{x}\right],\end{aligned} \tag{28}$$

where $x = E_{\nu_\mu}/E_\pi$, $\zeta = 1 - m_\mu^2/m_\pi^2$, and $f_{\nu_\mu^{(1)}}(x)$ and $f_{\nu_\mu^{(2)}}(x)$ are spectra of muonic neutrinos produced by the decay of pions and secondary muons, respectively. The function $f_{\nu_\mu^{(2)}}(x)$ is normalized as $\int_0^1 f_{\nu_\mu^{(2)}}(x)dx = 1$. The muonic neutrinos from the decay of an ultra-relativistic pion are evenly distributed within $0 < E_{\nu_\mu} \leqslant \zeta E_\pi$.

Similarly, for electronic neutrinos, we have

$$\varepsilon_{\nu_e}(E_{\nu_e}) = E_{\nu_e}\int_0^1 f_{\nu_e}(x) q_\pi^\pm\left(\frac{E_{\nu_e}}{x}\right)\frac{dx}{x}, \tag{29}$$

where $x = E_{\nu_e}/E_\pi$. The approximate expressions for $f_{\nu_\mu^{(1)}}(x)$, $f_{\nu_\mu^{(2)}}(x)$, and $f_{\nu_e}(x)$ are given in Kelner et al. (2006; see Appendix A). Note that those expressions only valid for the decay of relativistic pions ($E_\pi \gg m_\pi c^2$). Since we are interested in the reacceleration of $\sim$100 MeV CREs, we do not use them for the injection of secondary electrons/positions (Equation (11)) but for the emission of high-energy neutrinos.

Surface brightness or intensity for an optically thin source is obtained by integrating the emissivity along the line of sight. Now we assume that the Coma cluster has spherical symmetry, and the observed surface brightness at projected radius r is written as (see, e.g., Equation (2.12) of Murase & Beacom 2013)

$$B_\nu(\nu, r) = \frac{2}{(1+z)^3}\int_r^{r_{200}} \frac{dr'}{\sqrt{1 - r^2/r'^2}}\varepsilon(\nu', r'), \tag{30}$$

where $\nu' = (1+z)\nu$, and z is the redshift of the source. The observed flux is obtained by integrating the intensity with respect to the solid angle,

$$F_\nu(\nu) = 2\pi\int_0^{\theta_0} d\theta \sin\theta\cos\theta B_\nu(\nu, r(\theta)), \tag{31}$$

where $\theta = r/D_A$ is the angular size corresponding to radius r, $\theta_0 = r_{\rm ap}/D_A$, D_A is the angular diameter distance of the source, and $r_{\rm ap}$ is the assumed aperture radius at each wavelength. We take $r_{\rm ap} = 0.525$, 1.2, and 2.0 Mpc for the radio (e.g., Pizzo 2010; Brunetti et al. 2017), nonthermal X-rays (Wik et al. 2011), and gamma-rays (Ackermann et al. 2016a), respectively. We take $r_{\rm ap} = r_{200} \approx 2.3$ Mpc (Reiprich & Bohringer 2002) for neutrinos. We always use r_{200} as the maximum value for the integral region of Equation (30), regardless of $r_{\rm ap}$. Total radiated luminosity becomes

$$L = 4\pi D_L^2 \int d\nu F_\nu, \tag{32}$$

Table 1
Model Parameters

Parameter	Symbol	Definition
Reacceleration index	q	Equation (24)
Duration of the reacceleration	$t_{\rm R}$	Section 2.6
Primary electron ratio	$f_{\rm ep}$	Equation (19)
Normalization of the injection	$C_{\rm p}^{\rm inj}$	Equation (18)
Injection spectral index	α	Equation (18)
Radial dependence of the injection	$K(r)$	Equation (18)

where $D_{\rm L} = (1+z)^2 D_{\rm A}$ is the luminosity distance, and $z = 0.0232$ and $D_{\rm L} \approx 103$ Mpc for the Coma cluster (e.g., Abell et al. 1989). Gamma-ray photons that travel across the cosmological distance interact with the extragalactic background light (EBL) photons at IR and optical wavelengths, and they are attenuated by the $\gamma + \gamma \rightarrow e^+ + e^-$ process. The optical depth of $\gamma\gamma$ interaction, $\tau_{\gamma\gamma}(E_\gamma, z)$ depends on the energy of gamma-ray photons and the redshift of the source. The observed gamma-ray flux becomes

$$F_\gamma^{\rm obs} = F_\gamma^{\rm int} \exp(-\tau_{\gamma\gamma}(E_\gamma, z)), \quad (33)$$

where $F_\gamma^{\rm int}$ is the intrinsic gamma-ray flux. We adopt the table for $\tau_{\gamma\gamma}(E_\gamma, z)$ provided in Domínguez et al. (2011).

2.6. Initial Condition

In our calculation, we first prepare an initial CR distribution, which corresponds to the "radio-quiet" state, where the radio flux is too faint to be observed. To prepare an initial quiet state for each model, we integrate the FP equations (Equations (1) and (5)) without reacceleration (i.e., $D_{pp} = 0$) for a duration of t_0. In this paper, we take $t_0 = 4$ Gyr, regardless of the model parameters. This corresponds to the assumption that the injection starts from $z \sim 0.45$ and the amount of CRs before that epoch is negligible. The value of t_0 affects the injection rate of primary CRs. The cooling timescale of CREs takes maximum value of $\sim$1 Gyr at $E \approx 100$ MeV, and t_0 should be longer than that timescale to obtain a relaxed spectrum of seed CREs in the "radio-quiet" state. Besides, t_0 should be smaller than the age of a cluster; $t_0 \lesssim 10$ Gyr.

After this injection phase, the reacceleration in the ICM is switched on and lasts until the current "radio-loud" state is achieved. We use $t_{\rm R}$ as the elapsed time after the reacceleration is switched on. We assume that the present luminosity of the RH is still increasing, so $t = t_0 + t_{\rm R}$ corresponds to the current state. Considering the bimodality of the cluster population (Section 1), we refer to the state at $t \leqslant t_0$ as the "quiet" state and the state at $t_0 < t < t_0 + t_{\rm R}$ as the "loud" state. The primary injections, $Q_{\rm p}$ and $Q_{\rm e}^{\rm pri}$, are assumed to be constant throughout the calculation. In this work, we focus on the evolution of the CR distribution through the diffusion and resulting emission at the current state of the cluster, so we fix the properties of the cluster, e.g., the magnetic field (Equation (20)) and thermal gas density (Equation (3)), although they would be considerably disturbed by the merger activity.

2.7. Model Parameters

In Table 1, we summarize our model parameters. We test two types of the reacceleration with different q as explained in the previous section. The duration of reacceleration, $t_{\rm R}$ or $t_{\rm R}/\tau_{\rm acc}$, affects the spectrum of both synchrotron and gamma-ray radiation (Section 3.2). The parameter $t_{\rm R}$ should be chosen to explain the break appearing in the radio spectrum.

In this paper, we fix $\tau_{\rm acc} = 260$ Myr for the hard-sphere type reacceleration ($q = 2$) and $\tau_{\rm acc} = 100$ Myr for the Kolmogorov-type reacceleration ($q = 5/3$). As long as the acceleration timescale is in the range of $150 \lesssim \tau_{\rm acc} \lesssim 500$ Myr, the hard-sphere model can reproduce the radio spectrum by tuning other parameters like α, $C_{\rm p}^{\rm inj}$, and $t_{\rm R}$.

Concerning the injection of primary CRs, we have three parameters and one unknown function. We test two extreme cases for primary CREs: the primary-dominant case ($f_{\rm ep} = 0.01$) and the secondary-dominant case ($f_{\rm ep} = 0$). The energy spectrum of the primary CRs is modeled with Equation (18). We test four cases for the injection spectral index: $\alpha = 2.0$, 2.1, 2.2, and 2.45. The normalization $C_{\rm p}^{\rm inj}$ is determined from the absolute value of the observed flux at 350 MHz. The radial dependence of the injection $K(r)$ is constrained from the surface brightness profile of the RH.

We fix the strength and radial profile of the magnetic field, adopting the best-fit value from Bonafede et al. (2010): (B_0, η_B) = (4.7 μG, 0.5).

3. Results

In this section, we show the evolution of the CR distribution and nonthermal radiation from the Coma RH by integrating the FP equations. Example results for the time evolution of the spectra are shown in Section 3.1. The constraints on the model parameters from radio and gamma-ray observations are discussed in Section 3.2. The fluxes of high-energy radiation, including hard X-rays, gamma-rays, and neutrinos, are shown in Section 3.3 for the hard-sphere type acceleration and in Section 3.4 for the Kolmogorov type. We discuss the diffusive escape of high-energy CRPs in Section 3.5.

3.1. Overview of the Time Evolution of Cosmic-Ray Spectra

Figure 2 shows example results for a model with a given injection profile $K(r)$; (we will explain how this function is determined later on), the primary-dominant injection ($f_{\rm ep} = 0.01$), the hard-sphere type reacceleration ($q = 2$), and the injection spectral index of $\alpha = 2.0$. Before reacceleration starts, the CRE spectrum (dashed line in the left top panel) has a shape characterized by a single bump, reflecting the energy dependence of the cooling time shown in Figure 1. The cooling of low-energy CREs is dominated by the Coulomb collisions with thermal particles (Equation (7)), while radiative cooling dominates at higher energies. The maximum cooling time of CREs appears at energies of $\sim$100 MeV. The radio data are taken from Brunetti et al. (2013). The green empty points at 2.7 and 4.8 GHz show the flux corrected for the decrement due to the thermal SZ effect.

The reacceleration lifts the bump up to the energy at which the acceleration balances the cooling. This energy can be found in Figure 1 as a cross-point of the timescales of those processes, and it is $\sim$2 GeV for the hard-sphere model with $\tau_{\rm acc} =$ 260 Myr. This shift of the bump shape affects the resulting radio spectrum (left bottom). The adequate choice of $\tau_{\rm acc}$ makes a break of the spectrum around a few GHz. In other words, $\tau_{\rm acc} \approx 300$ Myr is required to fit the observed spectra when CRs are injected with a single power-law spectrum.

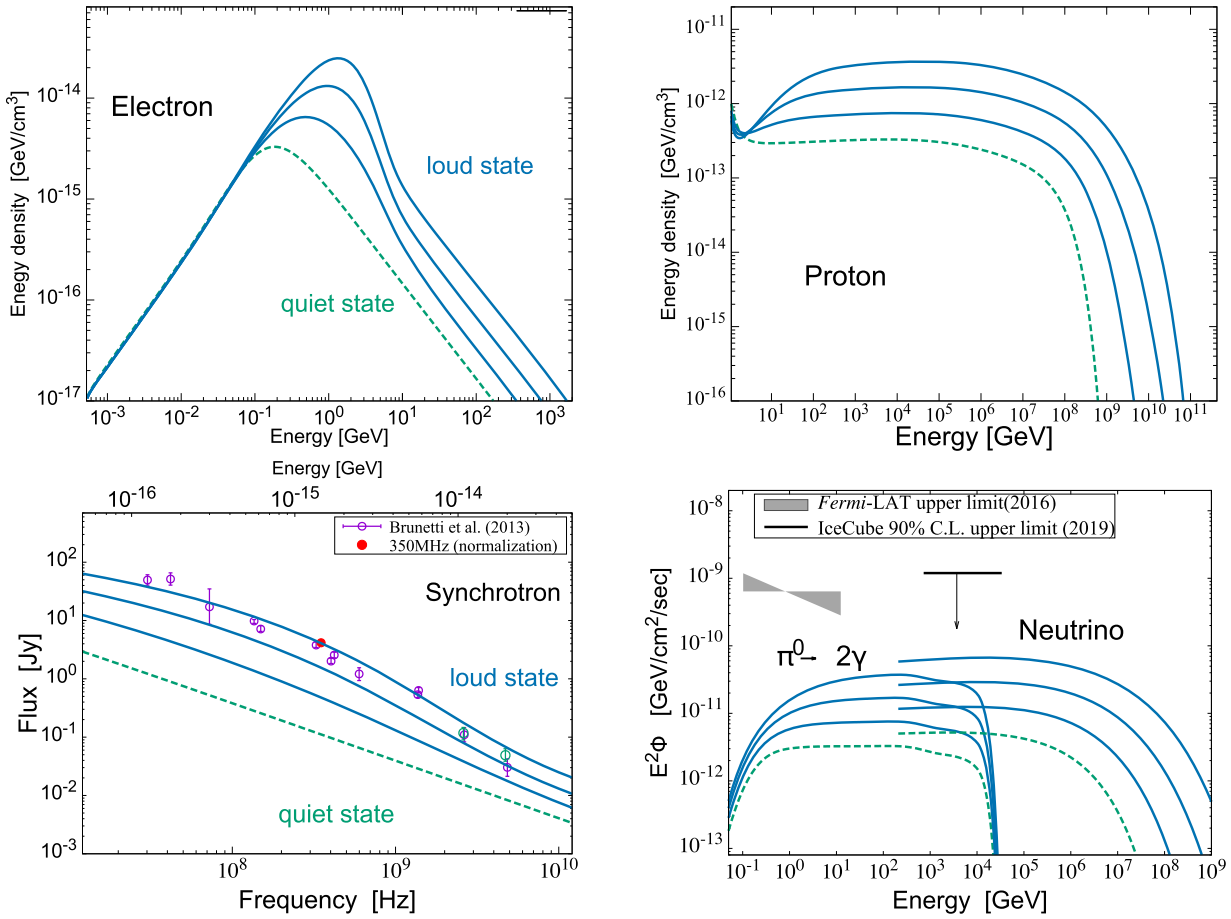

Figure 2. Time evolution of the CR energy distributions (top) and corresponding radiation (bottom) for an example case with $B_0 = 4.7\ \mu$G, $\eta_B = 0.5$, the hard-sphere type acceleration ($q = 2$), and the injection spectral index $\alpha = 2.0$ in the primary-dominant scenario ($f_{\rm ep} = 0.01$). The CR spectra are averaged within the core radius $r \leqslant r_{\rm c} = 290$ kpc. The aperture radii $r_{\rm ap}$ used to calculate the emission fluxes are different for each radiation type: $r_{\rm ap} = 525$ kpc for synchrotron, 2.0 Mpc for π^0 gamma-ray, and r_{200} for neutrinos. In each figure, from bottom to top, the spectra at $t_{\rm R} = 200$, 400, and 500 Myr are shown with solid curves. The spectra before reacceleration ($t_{\rm R} = 0$ Myr) are shown with dashed curves. Left panels: the CRE and synchrotron spectra. Right panels: the spectra of CRPs and hadronic radiation. The neutrino fluxes are the sum of the ones of all flavors. In the right bottom panel, the results are compared with upper limits given by Fermi-LAT and IceCube (see the main text for details). The neutrino spectra below 300 GeV are not shown to improve visibility.

However, the spectral shape of CRPs remains a single power law with an exponential cutoff, since CRPs do not suffer significant cooling and the acceleration timescale of the hard-sphere reacceleration does not depend on the momentum of particles (Section 2.4). The maximum energy reaches 10^{19} eV within $t_{\rm R} \lesssim 500$ Myr. The spectra of gamma-rays and neutrinos follow the evolution of the CRP spectrum and resulting fluxes are about one order of magnitude larger than those in the quiet state.

In the Kolmogorov model ($q = 5/3$), the acceleration timescale is longer for higher-energy particles (Equation (25)), so CRPs above $\sim$1 TeV are not efficiently reaccelerated within the reacceleration phase of $t_{\rm R} \lesssim 1$ Gyr. Thus, the predicted fluxes of hadronic emission and escaping high-energy CRPs become much lower than for the hard-sphere model (see Section 3.4).

3.2. Constraints on Model Parameters

In the following, we show constraints on the duration of the reacceleration phase $t_{\rm R}$ and the radial profile of the primary CR injection, $K(r)$. In our calculation, $t_{\rm R}$ is mainly constrained by the RH spectrum. Figure 3 (left) shows the $t_{\rm R}$ dependence of the shape of the synchrotron spectrum. In this figure, the primary CR injection rate is adjusted to realize the observed flux at 350 MHz for each $t_{\rm R}$ so that we can compare the shape of the spectrum for different $t_{\rm R}$. The flux, in practice, increases with time as shown in Figure 2 (bottom left). The dashed line in Figure 3 represents the case without reacceleration (pure-secondary model), which is in tension with the observed break at 1 GHz. Note that the aperture radius assumed in radio data is not strictly constant with frequency. The tension in the single power-law model would be relaxed when a much softer injection index ($\alpha \approx 2.8$) is adopted and the normalization is not anchored to the flux at 350 MHz.

The parameters that affect the spectral shape are the injection index α, parameters for the reacceleration, $\tau_{\rm acc}$ and $t_{\rm R}$, and the amount of primary CREs, $f_{\rm ep}$. The radio flux is mostly contributed by CREs in the core region, $r \leqslant r_{\rm c}$, where the magnetic field is relatively strong. Hence the radial dependence of the injection, $K(r)$, dose not greatly affect the radio spectrum.

The upper limit on gamma-ray flux gives another constraint on the $t_{\rm R}$. In Figure 3 (right), we show the gamma-ray fluxes normalized by the radio flux of 350 MHz at each $t_{\rm R}$. As discussed in Brunetti et al. (2017), the "pure-secondary model" ($t_{\rm R} = 0$ and $f_{\rm ep} = 0$) is in tension with the limit from Fermi-LAT data when $(B_0,\ \eta_B) = (4.7\ \mu$G, 0.5). In order to relax the tension, the magnetic field is required to be $\sim$10 times larger than the one we adopted. In general, the spectrum of CREs

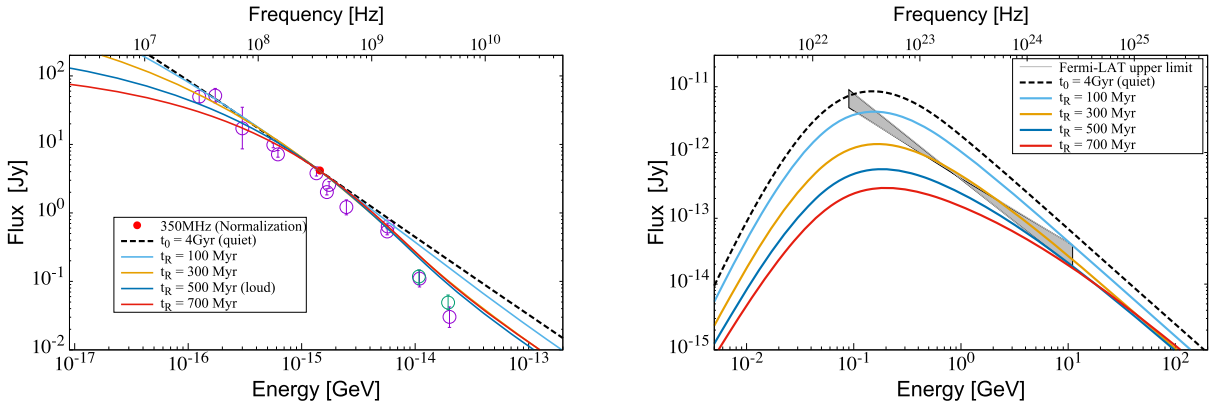

Figure 3. Normalized spectra of the RH (left) and gamma-rays from π^0 decay (right) for various t_R (the elapsed time of the reacceleration phase) for no primary case ($f_{ep} = 0$) with hard-sphere type reacceleration ($q = 2$). The model parameters used here are the same as in Figure 2. At each t_R, the radio flux at 350 MHz is used to normalize the gamma-ray flux. The black dashed line shows the result of the pure-secondary model, where $t_R = 0$. The data points on the left panel are taken from Brunetti et al. (2017). The gamma-ray fluxes on the right panel are compared with the Fermi-LAT limit from Ackermann et al. (2016a).

above $\sim$100 MeV is softer than that of CRPs because high-energy electrons quickly lose their energies through radiation, so the relative increase of the energy density of radio-emitting CREs due to reacceleration is larger than that for gamma-ray-emitting CRPs. Because of this, the ratio between the fluxes of radio and gamma-ray, $F_{\rm radio}/F_\gamma$, increases with $t_R/\tau_{\rm acc}$, so the upper limit on F_γ gives the lower bound for t_R. From this figure, for example, $t_R \gtrsim 400$ Myr is required from the gamma-ray upper limit.

Our model should also reproduce the observed surface brightness profile of the RH (e.g., Brown & Rudnick 2011). The current spatial distribution of CREs is the consequence of the combined effects of various processes: primary injection, spatial diffusion, and secondary injection from inelastic *pp* collisions, so we need to follow the diffusive evolution of CR distributions with a modeled injection that persists over several Gyrs.

In the secondary-dominant model, the injection rate of CREs is proportional to the product of the densities of parental CRPs and thermal protons. Brunetti et al. (2017) pointed out that the ratio of the CRP energy density to the thermal energy density needs to increase with radius to reproduce the broad profile of the radio surface brightness of the Coma RH, considering the gamma-ray upper limit given by Fermi-LAT. This may suggest that the injection of CRs occurs at peripheral regions rather than the central region, where the thermal gas density is relatively large.

Since both Coulomb and synchrotron coolings are weaker at larger r, the relative increase of the synchrotron emissivity due to reacceleration is more prominent at larger r. Thus, the surface brightness profile becomes broad with t_R.

We have tested various injection profiles and confirmed that those biased to the center, for example, $K(r) \propto \delta(r)$ or $K(r) \propto 4\pi r^2 n_{\rm th}$, are rejected if D_{pp} is constant with radius. Such profiles do not produce extended halo emission but small core emission. Figure 4 shows the surface brightness profile of the RH and the corresponding CRE distribution. The CRE distribution needs to be roughly uniform within $r \lesssim 1$ Mpc. The two-peaked feature in the spatial distribution of the CREs is caused by a combination of the injection profile of primary CRPs (Figure 5 left) and the cored profile of the ICM (Equation (3)).

Since the giant RH extends up to 1 Mpc from the center, a sufficient amount of primary CRs should be supplied outside the cluster core. Especially in the secondary-dominant scenario, the density of the primary CRPs should increase with r and have a peak at $\sim$1 Mpc to realize the CRE distribution shown in Figure 4. Such a profile of CRPs could originate from an injection from the shock waves induced by the cluster formation process, such as mergers of clusters or mass accretion. Considering the injection from a shock front located at $r \sim r_{\rm m}$ and internal sources such as AGNs, we use the following expression of $K(r)$ for the secondary-dominant model ($f_{ep} = 0$):

$$K_1(r) = 4\pi r^2 \left[\frac{c_1}{\sqrt{2\pi}\,\sigma} \exp\left[-\frac{(r - r_{\rm m})^2}{2\sigma^2} \right] + c_2 n_{\rm th}(r) \right]. \quad (34)$$

The component proportional to $n_{\rm th}$ represents the injection from internal sources. The factor $4\pi r^2$ is introduced to convert the volume density into the linear density. We find that typical values of the parameters are $c_1/c_2 \simeq 3.5 \times 10^{-2}$ Mpc cm^{-3}, $r_{\rm m} \simeq 1.3$ Mpc, and $\sigma \simeq 0.45$ Mpc. The values of those parameters adopted in our calculations are summarized in Table 2.

The appropriate choice of t_R and $K(r)$ should be changed when primary electrons are present. In the primary-dominant case, $K(r)$ is roughly proportional to the current distribution of the CREs (Figure 4, right), since the radial diffusion of $\sim$GeV CREs is not efficient. Hence, the injection profile needs to be nearly uniform within $\sim$1 Mpc:

$$K_2(r) = r^\delta \exp\left[-\left(\frac{r}{r_{\rm cut}} \right)^\delta \right]. \quad (35)$$

This functional shape implies $\frac{dK_2}{dr} = 0$ at $r_{\rm cut}$, which means that CRs are typically injected at around $r \sim r_{\rm cut}$ even in the primary-dominant model. This may suggest that primary sources are distributed over the halo volume, or the injection radius shifts with time to achieve the above functional shape just before the onset of reacceleration. The typical values of the parameters are $\delta \simeq 2$ and $r_{\rm cut} \simeq 1.2$ Mpc (Table 3).

Figure 5 shows the radial dependence of the injection density of primary CRPs for models with hard-sphere reacceleration and $\alpha = 2.45$. Those profiles are derived under the assumption that the efficiency of the acceleration, or $\tau_{\rm acc}$, is constant with r. If $\tau_{\rm acc}$ decreases with radius, the CR injection profile can be

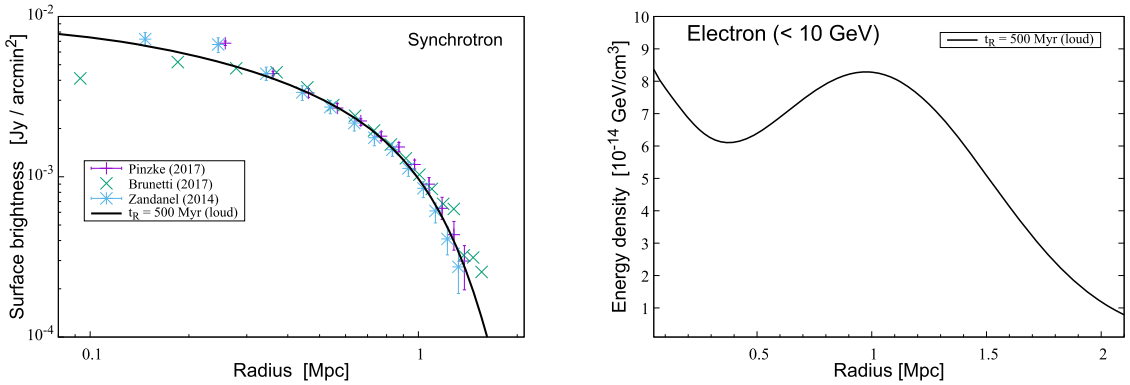

Figure 4. Left: radio surface brightness profile at 350 MHz for the same model as in Figures 2 and 3, i.e., the secondary-dominant model with the hard-sphere reacceleration, $B_0 = 4.7\ \mu$G, and soft injection $\alpha = 2.45$. The data points on the left panel are taken from various papers (Zandanel et al. 2014; Brunetti et al. 2017; Pinzke et al. 2017), which are originally based on the same Westerbork Synthesis Radio Telescope (WSRT) observation (Brown & Rudnick 2011). Right: radial distribution of the CRE energy density in the same calculation as in the left panel. To clarify the connection with radio emission, only CREs of energy less than 10 GeV are considered here.

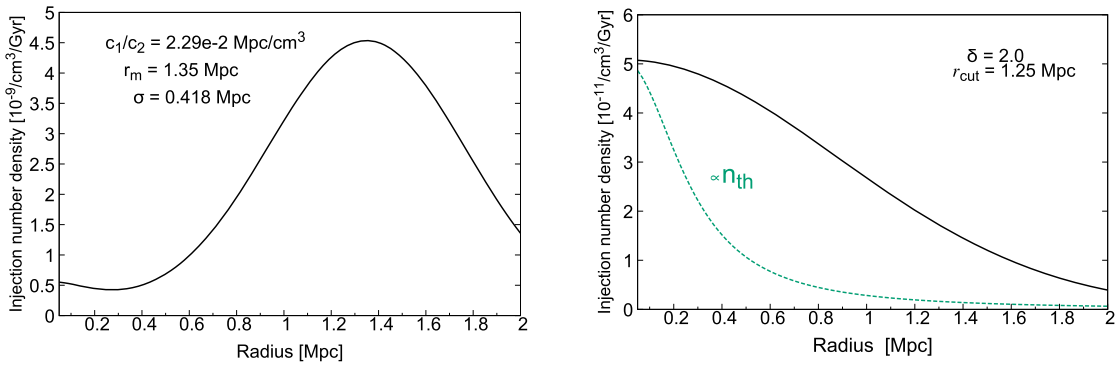

Figure 5. Primary CRP injection profiles as a function of radial distance for $f_{ep} = 0$ (left) and $f_{ep} = 0.01$ (right). The hard-sphere reacceleration ($q = 2$) with $B_0 = 4.7\ \mu$G and $\alpha = 2.45$ is assumed here. The dashed line in the right figure shows a profile proportional to the thermal gas density.

Table 2
Parameters for the Secondary-dominant Models ($f_{ep} = 0$)

q	α	t_R (Myr)	c_1/c_2 (Mpc cm^{-3})	r_m (Mpc)	σ (Mpc)	$L_p^{inj}(>10$ GeV) (erg s^{-1})
2	2.0	400	3.65×10^{-2}	1.39	0.418	1.9×10^{45}
(hard-sphere)	2.1	400	3.65×10^{-2}	1.38	0.418	7.4×10^{44}
	2.2	400	3.32×10^{-2}	1.35	0.418	5.4×10^{44}
	2.45	500	2.29×10^{-2}	1.35	0.418	1.7×10^{44}
5/3	2.0	180	4.11×10^{-2}	1.55	0.474	9.7×10^{44}
(Kolmogorov)	2.1	160	4.11×10^{-2}	1.55	0.474	8.4×10^{44}
	2.2	160	4.63×10^{-2}	1.55	0.474	5.9×10^{44}
	2.45	160	2.29×10^{-2}	1.25	0.418	1.7×10^{44}

Note. Parameters c_1, c_2, r_m and σ are for $K_1(r)$; (Equation (34)).

more concentrated in the center (e.g., Pinzke et al. 2017; Adam et al. 2021).

The normalization of the injection is determined from the observed radio flux at 350 MHz. Once the model parameters, α, $K(r)$, and C_p^{inj}, are given, the luminosity of the CR injection can be calculated by integrating Equation (18) over r and p. The injection luminosity above 10 GeV is also shown in Tables 2 and 3. Above that energy, CRPs are not significantly affected by Coulomb cooling, so they lose their energies mainly through pp collisions and diffusive escape. The required luminosity ranges from $L_p^{inj} \sim 10^{41}$ erg s^{-1} to 10^{45} erg s^{-1}.

The fiducial value of the luminosity adopted in previous studies (e.g., Murase et al. 2008; Kotera et al. 2009; Kushnir & Waxman 2010; Fang & Olinto 2016; Fang & Murase 2018; Hussain et al. 2021) is $L_p^{inj} \sim 10^{44} - 10^{45}$ erg s^{-1}. The injection power of our secondary-dominant model ($f_{ep} = 0$) is comparable to those values. Note the additional energy injection from the turbulent reacceleration in our model. The hard-sphere reacceleration makes the energy density of CRs about ten times larger (see also Figure 6), so we need about ten times larger injection power in the pure-secondary model, where the reacceleration is absent.

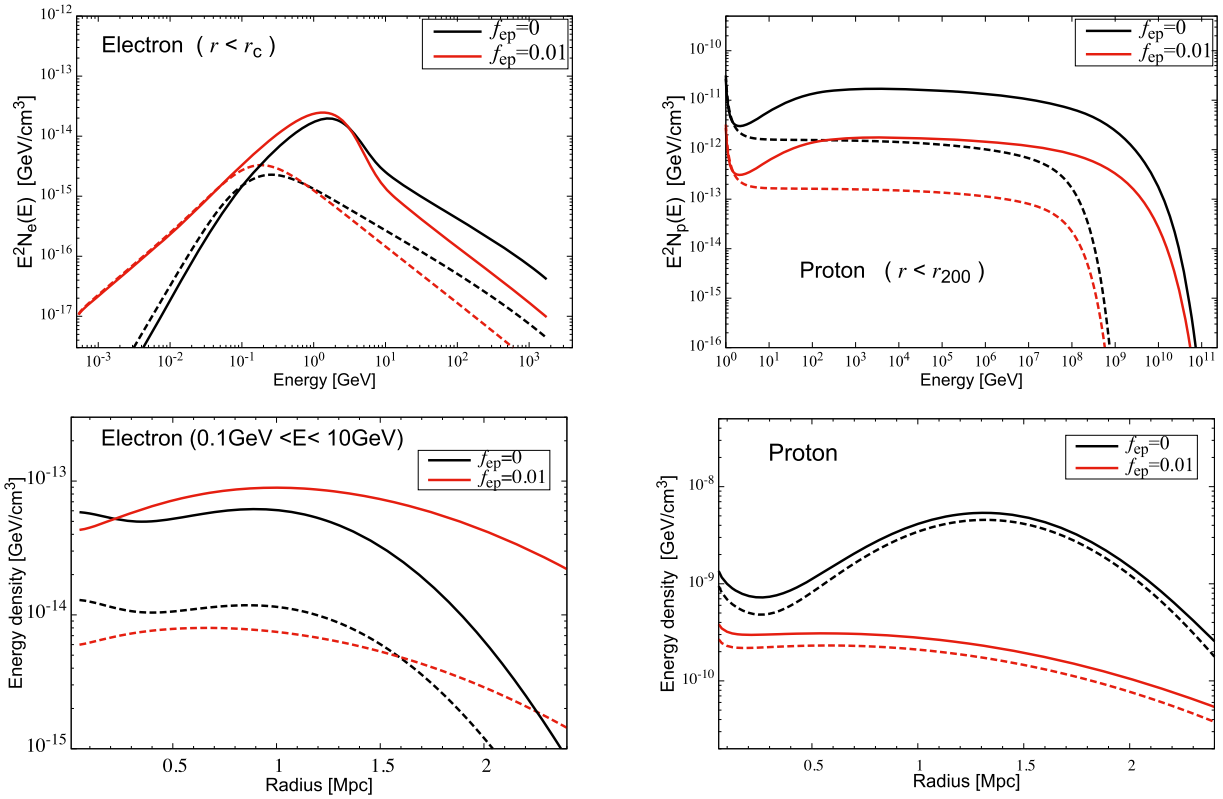

Figure 6. CR energy density distribution as a function of energy (top) and radial distance (bottom) for the hard-sphere model with $B_0 = 4.7\ \mu$G and $\alpha = 2.0$. The results for CREs and CRPs are shown in the left and right panels, respectively. The results for the secondary-dominant case ($f_{\rm ep} = 0$) are shown in black and those for the case with $f_{\rm ep} = 0.01$ are in red. The "loud" and "quiet" states correspond to the solid and dashed curves, respectively. The CRE spectra (top left) are averaged within $r \leqslant r_{\rm c}$, while the CRP spectra (top right) are averaged within $r \leqslant r_{200}$. In the left bottom panel, the spectrum of CREs is integrated between $0.1 \leqslant E \leqslant 10$ GeV to show the radial distribution of radio-emitting CREs.

Table 3
Parameters for the Primary-dominant Models ($f_{\rm ep} = 0.01$)

q	α	$t_{\rm R}$ (Myr)	$r_{\rm cut}$ (Mpc)	δ	$L_{\rm p}^{\rm inj}(>10{\rm GeV})$ (erg s^{-1})
2	2.0	600	1.70	2.3	5.6×10^{43}
(hard-sphere)	2.1	600	1.70	2.1	2.0×10^{43}
	2.2	600	1.60	2.1	8.7×10^{43}
	2.45	800	1.25	2.0	5.9×10^{41}
5/3	2.0	240	1.40	2.0	1.0×10^{43}
(Kolmogorov)	2.1	240	1.30	1.9	1.6×10^{42}
	2.2	240	1.25	1.9	5.6×10^{41}
	2.45	240	1.15	1.8	5.1×10^{40}

Note. Parameters $r_{\rm cut}$ and δ are for $K_2(r)$; (Equation (35)).

The injections required in primary-dominant models ($f_{\rm ep} = 0.01$) are much smaller. The injection luminosity of $L_{\rm p}^{\rm inj} \gtrsim 10^{45}$ erg s^{-1} overproduces the observed radio luminosity even without reacceleration.

3.3. Hard-sphere Type Acceleration

Hereafter in this section, we discuss multiwavelength and neutrino emission from the Coma cluster based on the model for the RH explained above. The results for each model are summarized in the tables below (Tables 4 and 5). First, we show the results for the hard-sphere type acceleration, $q = 2$. In this case, all CRs have the same $t_{\rm acc}$ regardless of their energies. That reacceleration produces high-energy CRPs more efficiently, and the emissivities of the hadronic emission become larger than for the Kolmogorov reacceleration.

The resulting CR distributions are shown in Figure 6. The top panels show the energy spectra of CREs and CRPs, while the bottom panels show their spatial distributions.

Primary CREs are distributed down to trans-relativistic energies ($E_{\rm e} \simeq 0.1 m_{\rm e}c^2$), while secondary CREs with energies less than $1/10$ of the pp threshold energy $E_{\rm th}$ are hardly produced. That causes the difference in the CRE spectra (top left panel) below 100 MeV between $f_{\rm ep} = 0$ and $f_{\rm ep} = 0.01$.

We normalize the results using the synchrotron flux at 350 MHz, and this frequency corresponds to the electron energy of $E_{\rm e} \simeq 2.6$ GeV for $B = 4.7\ \mu$G. Thus, the amount of CREs at 2.6 GeV should be the same in all models at the radio-loud state. In reality, there is a small deviation at that energy, which may arise from the difference in the radial distribution of CREs (left bottom panel, see also Figure 4). The energy density of $\sim 5 \times 10^{-14}$ GeV cm^{-3} is in good agreement with other studies with the same assumption about the magnetic field (e.g., Adam et al. 2021).

The radial diffusion slightly flattens the distributions of CRPs (bottom right) compared to the injection profile, $K(r)$. That said, CREs are more concentrated toward the cluster center for $f_{\rm ep} = 0$, because the production of the secondary CREs is more efficient at smaller radius. This difference in radial distribution between CRPs and CREs is relatively small for $f_{\rm ep} = 0.01$, since the distribution of primary CREs is not affected by the density profile of the ambient ICM. Figure 7 shows the overall spectrum of the nonthermal electromagnetic and all-flavor neutrino emission together with the observational

Table 4
Predicted Neutrino and Gamma-ray Fluxes Together with the Luminosity of Escaping CRPs, for the Hard-sphere Models ($q = 2$) with $\tau_{\rm acc} = 260$ Myr and (B_0, η_B) = (4.7 μG, 0.5)

$f_{\rm ep}$[a]	α	$E_\nu F_\nu$(loud)[b] (GeV cm^{-2} s^{-1})	$E_\nu F_\nu$(quiet)[c] (GeV cm^{-2} s^{-1})	$E_\gamma F_\gamma$(loud)[d] (GeV cm^{-2} s^{-1})	L_ν[e] (erg s^{-1})	$L_{\rm CRP}(>10^{17}$ eV)[f] (erg s^{-1})	$L_{\rm CRP}(>10^{18.5}$ eV)[f] (erg s^{-1})
0	2.0	4.1×10^{-10}	4.3×10^{-11}	2.2×10^{-10}	6.6×10^{42}	6.4×10^{44}	1.3×10^{43}
	2.1	1.3×10^{-10}	7.1×10^{-12}	2.0×10^{-10}	2.5×10^{42}	1.7×10^{44}	3.1×10^{42}
	2.2	5.3×10^{-11}	8.2×10^{-12}	3.1×10^{-10}	1.0×10^{42}	4.7×10^{43}	4.8×10^{41}
	2.45	2.7×10^{-12}	6.3×10^{-14}	3.7×10^{-10}	1.1×10^{41}	1.9×10^{42}	3.9×10^{40}
0.01	2.0	5.7×10^{-11}	2.4×10^{-12}	2.5×10^{-11}	8.4×10^{41}	8.9×10^{43}	7.6×10^{42}
	2.1	1.1×10^{-11}	3.7×10^{-13}	1.4×10^{-11}	2.1×10^{41}	1.6×10^{43}	1.2×10^{42}
	2.2	2.3×10^{-12}	6.1×10^{-14}	1.1×10^{-11}	5.7×10^{40}	3.0×10^{42}	1.7×10^{41}
	2.45	9.0×10^{-14}	2.2×10^{-16}	5.6×10^{-12}	3.3×10^{39}	6.1×10^{40}	8.6×10^{38}

Notes. The maximum energy of primary protons is assumed to be $E_{\rm p}^{\rm max} = 100$ PeV.
[a] The ratio of Primary CREs to primary CRPs defined in Equation (19).
[b] All-flavor neutrino flux at 1 PeV for the radio-loud state.
[c] The neutrino flux at 1 PeV for the radio-quiet state.
[d] Gamma-ray flux at 1 GeV for the radio-loud state.
[e] All-flavor neutrino luminosity integrated above 10 PeV.
[f] Luminosity of CRPs escaping from the virial radius of the cluster $r = r_{200} \approx 2.3$ Mpc of energy $E > 100$ PeV and $E > 10^{18.5}$ eV, respectively, at the radio-loud state.

Table 5
Same as Table 4, but for $q = 5/3$ (Kolmogorov), $\tau_{\rm acc} = 100$ Myr

$f_{\rm ep}$	α	$E_\nu F_\nu$(loud) (GeV cm^{-2} s^{-1})	$E_\gamma F_\gamma$(loud) (GeV cm^{-2} s^{-1})	L_ν (erg s^{-1})	$L_{\rm CRP}(>10^{17}$ eV) (erg s^{-1})	$L_{\rm CRP}(>10^{18.5}$ eV) (erg s^{-1})
0	2.0	3.5×10^{-11}	8.4×10^{-11}	3.1×10^{41}	1.1×10^{43}	1.7×10^{28}
	2.1	1.4×10^{-11}	1.3×10^{-10}	1.0×10^{41}	3.7×10^{42}	3.9×10^{27}
	2.2	3.5×10^{-12}	1.6×10^{-10}	3.3×10^{40}	8.3×10^{41}	6.4×10^{26}
	2.45	4.0×10^{-14}	1.6×10^{-10}	1.1×10^{39}	6.1×10^{39}	3.0×10^{24}
0.01	2.0	4.8×10^{-13}	2.0×10^{-12}	2.7×10^{40}	1.2×10^{41}	2.0×10^{26}
	2.1	3.6×10^{-14}	9.2×10^{-13}	4.8×10^{39}	7.7×10^{39}	9.7×10^{24}
	2.2	4.6×10^{-15}	6.0×10^{-13}	9.6×10^{38}	8.3×10^{38}	7.8×10^{23}
	2.45	2.7×10^{-17}	1.8×10^{-13}	1.6×10^{37}	1.6×10^{36}	1.2×10^{21}

Note. See Table 4 for the details of each quantity. The neutrino fluxes for the radio-quiet states are the same to two significant digits as radio-loud states.

data and upper limits. In the secondary-dominant models ($f_{\rm ep} = 0$), we can expect larger fluxes of hadronic emission than for the primary-dominant models ($f_{\rm ep} = 0$, Figure 8). Gamma-rays above ~TeV energies are attenuated by interactions with the EBL (Section 2.5). The cutoff shape appearing in the neutrino fluxes simply reflects the cutoff in the CRP spectra, so the flux above 1 PeV is sensitive to $E_{\rm p}^{\rm max}$ (Equation (18), see also Section 4.4). The upper limit on the neutrino flux in this figure is given by the point-source search with ten years of IceCube data (Aartsen et al. 2020a). That shows the median upper limit of the flux from the direction of the Coma cluster at a 90% confidence level. The angular extension of the Coma cluster is not considered here, because the extension is comparable to the angular resolution of muon track events (~1 deg at TeV energies; Murase & Beacom 2013). Our result is consistent with the lack of a significant excess of neutrino events from Coma (e.g., Aartsen et al. 2014).

A unique feature of our 1D calculation appears in the spectra of the leptonic radiation in Figure 7. In this model, the synchrotron spectrum does not fit the data well for any choice of $t_{\rm R}$ within $150 \leqslant t_{\rm R} \leqslant 500$ Myr. The resulting spectra are clearly harder than the observational data, especially at higher frequencies above 1.4 GHz. In the case of $\alpha = 2.0$, the radio spectral index at the quiet state (black dashed line) becomes $\alpha_{\rm syn} \approx -0.9$, while it is expected to be $\alpha_{\rm syn} = -1.0$ when the injection spectrum of secondary CREs follows $Q_{\rm e}^{\rm sec} \propto p^{-2.0}$. One of the possible causes of this spectral hardening is the energy-dependent diffusion of parental CRPs. Since most of the CRPs are injected outside the core (Figure 5) and the diffusion is faster for higher-energy CRPs ($t_{\rm diff} \propto E^{-1/3}$), the CRP spectra are harder in the core region than in the injection region. Secondary CREs also show hard spectra in the core region (Figure 6 top left), where the magnetic field is strong. To confirm this, we tested the case without radial diffusion ($D_{rr} = 0$, not shown in the figure) and found that the spatial diffusion actually hardens the CRE spectral index by ~0.05. The weak energy dependence in the *pp* cross section is another cause of the spectral hardening (Section 2.2). That makes the spectral index of $Q_{\rm e}^{\rm sec}$ above $\gamma_{\rm e} > 10^3$ harder by ~0.05 compared to the case of $\sigma_{pp} =$ Const. (e.g., Kelner et al. 2006).

Note that the brightness profile of the RH can also be explained by, e.g., the "*M*-turbulence" model of Pinzke et al. (2017), where the efficiency of the reacceleration increases with radius and the CR distribution is more concentrated toward the central region. In such models, the spectral hardening due to radial diffusion is not effective, and the tension between observed and calculated RH spectra could be relaxed (see also Section 4.1).

In the reacceleration phase, the flux above ~1 GHz, where the cooling timescale becomes shorter than the reacceleration

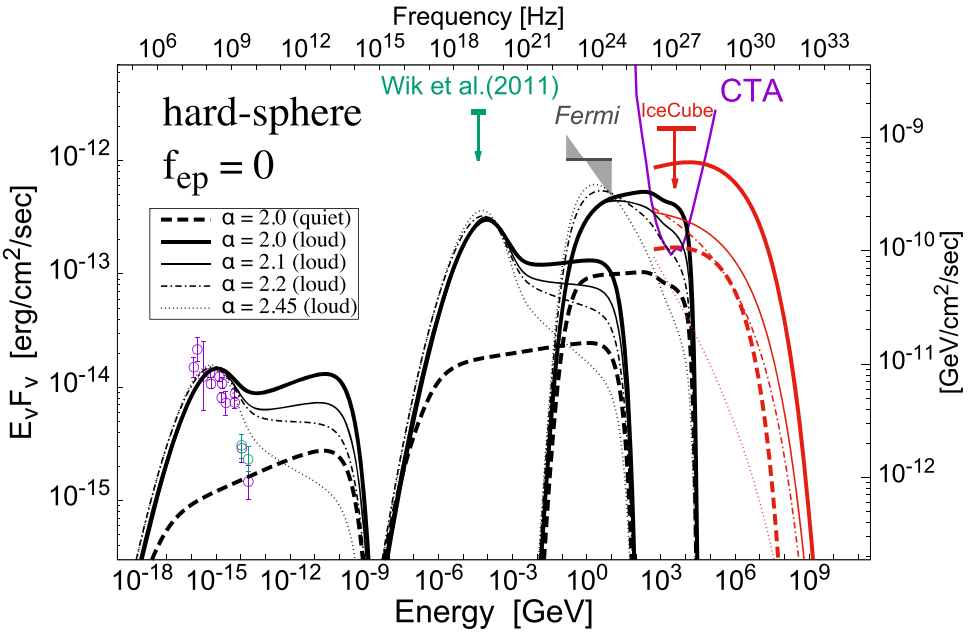

Figure 7. Nonthermal electromagnetic and all-flavor neutrino νF_ν spectra for the most optimistic cases, $q = 2$ and $f_{ep} = 0$. From left to right, synchrotron, inverse-Compton, and π^0 gamma emission are shown in black curves. The red curves show neutrino fluxes. The "loud" and "quiet" states are shown in the thick solid and thick dashed curves, respectively. The loud-state spectra for different α are also shown: $\alpha = 2.1$ (thin solid), 2.2 (thin dotted–dashed), and 2.45 (thin dotted). Note that each spectrum is calculated with a different aperture radius r_{ap} to compare with observations: $r_{ap} = 0.525$ Mpc and $= 1.2$ Mpc for synchrotron and ICS spectra, respectively, while that for gamma-rays is 2.0 Mpc. The high-frequency cutoffs of the leptonic radiation are artificial ones. The upper limits for hard X-rays, gamma-rays, and neutrinos are taken from Wik et al. (2011), Ackermann et al. (2015), and Aartsen et al. (2020a), respectively. The point-source sensitivity of the Cherenkov Telescope Array (CTA) with 50 hr of observation is drawn with a magenta line (adopted from https://www.cta-observatory.org/science/cta-performance/).

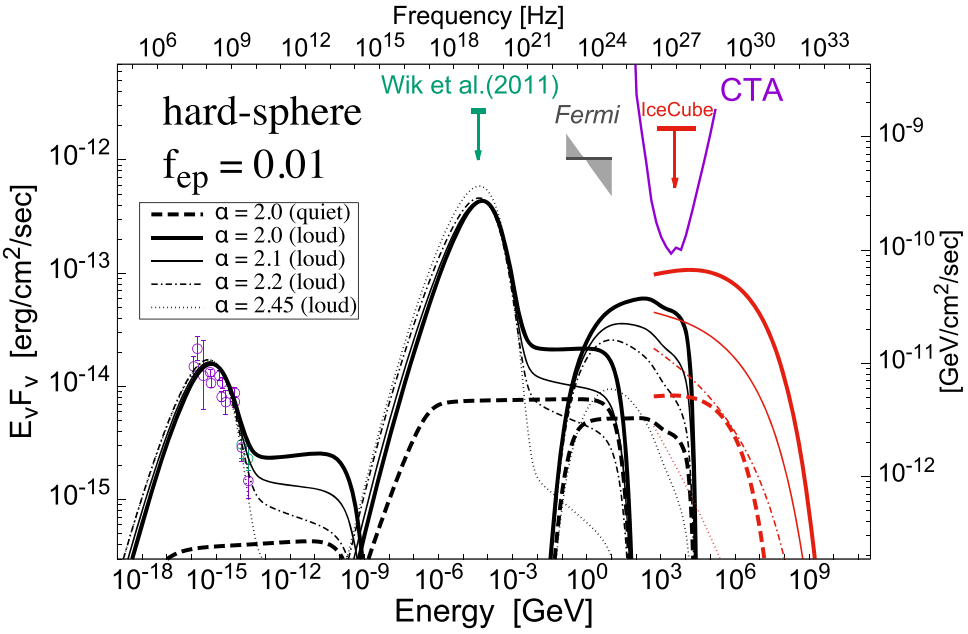

Figure 8. Multiwavelength and neutrino νF_ν spectra for $f_{ep} = 0.01$. Other parameters are the same as in Figure 7.

timescale, also increases with time, because the injection rate of the secondary CREs increases due to the reacceleration of CRPs.

The emissivity of ICS is independent of the cored structure of the galaxy cluster, so the resulting spectrum is softer than synchrotron. ICS from CREs contributes to the gamma-ray flux at 1 GeV up to 0.3 times as much as the emission from the decay of π^0. We did not solve the evolution of high-energy CREs with a Lorentz factor larger than $\gamma_e = 10^7$ to save the computation time, so the high-frequency cutoff shown in the leptonic radiation is an artificial one.

The radial and spectral distributions of CRs for the primary-dominant case ($f_{ep} = 0.01$) are shown in Figure 6 with red lines. In this case, the CRE spectrum becomes softer than for $f_{ep} = 0$, since the injection profile is nearly uniform within the RH and the CRE spectrum is not significantly affected by the spatial diffusion of CRPs. For all values of $\alpha = 2.0$, 2.1, 2.2, and 2.45, the radio spectrum can be reproduced with optimal

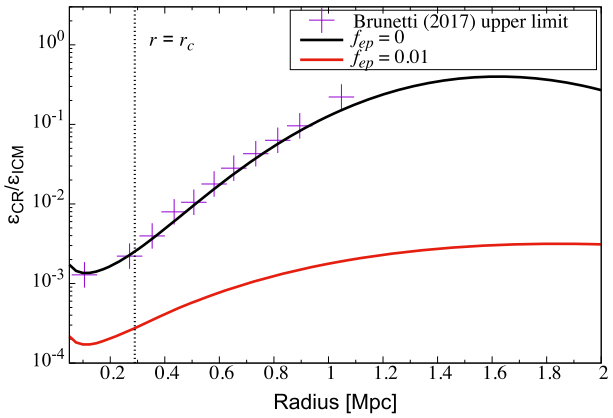

Figure 9. Radial dependence of the energy density ratio of CRPs $\epsilon_{\rm CR}$ to the thermal ICM $\epsilon_{\rm ICM}$. The results for the secondary-dominant model ($f_{\rm ep} = 0$) and the primary-dominant model ($f_{\rm ep} = 0.01$) are shown with black and red solid lines, respectively. We assumed $q = 2$ and $\alpha = 2.45$ in both models. The dotted line denotes the core radius $r_c = 290$ kpc. For comparison, we plot the upper limit for the CRP energy density given by Brunetti et al. (2017), which is derived from the gamma-ray upper limit for the model with $\tau_{\rm acc} = 260$ Myr, $t_{\rm R} = 720$ Myr, $B_0 = 4.7\ \mu$G, $\eta_B = 0.5$, and $\alpha = 2.45$.

values of $t_{\rm R}$ listed in Table 3. Therefore, the primary-dominant model is preferable to the secondary-dominant model unless a steeper index $\alpha \gtrsim 2.5$ or radially increasing D_{pp} is adopted.

The νF_ν fluxes for $f_{\rm ep} = 0.01$ are shown in Figure 8. The fluxes of hadronic emission are about one order of magnitude smaller than for the secondary-dominant cases. They are well below the upper limits, so $t_{\rm R}$ is constrained solely by the shape of the radio spectrum. The ICS spectrum around 100 keV is almost the same as for the secondary-dominant case, since the leptonic radiation is constrained by the radio flux (see also Section 4.2.2).

In Table 4, we summarize PeV neutrino fluxes for each α together with the fluxes of π^0 gamma-rays and escaping CRPs (Section 3.5).

The models with smaller α, i.e., harder injection, naturally predict larger neutrino fluxes. When the amount of CREs is constrained by the luminosity of the RH, less hadronic emission is predicted with a larger $f_{\rm ep}$. The neutrino flux for $f_{\rm ep} = 0.01$ is smaller by about one order of magnitude than for $f_{\rm ep} = 0$ (Table 4). The luminosity of escaping CRs shown here is the one from the loud state. This luminosity is powered by the reacceleration, and it strongly depends on $t_{\rm R}/\tau_{\rm acc}$ and $E_{\rm p}^{\rm max}$ (see Section 3.5). This luminosity can be comparable to the injection luminosity $L_{\rm p}^{\rm inj}$ listed in Tables 3 and 2, since the power of the reacceleration $P_{\rm reacc} \sim 10^{42}$–$10^{47}$ erg s^{-1}, depending on the parameters, can dominate the injection power.

Figure 9 shows the radial dependence of the energy density ratio of CRPs to the thermal ICM, $\epsilon_{\rm CR}/\epsilon_{\rm ICM}$, for models with two different $f_{\rm ep}$. In both cases, the ratio increases with radius. Many previous studies have pointed out a similar trend, using a semi-analytical argument (Keshet 2010; Fujita et al. 2013) or by post-processing cosmological simulations (Pfrommer 2008). The purple points in Figure 9 show the upper limits given by Brunetti et al. (2017) using the Fermi upper limit (Ackermann et al. 2016a), and our results are consistent with these limits. The model of Brunetti et al. (2017) is basically similar to our secondary-dominant hard-sphere model (their parameters are summarized in the caption of Figure 9), but the spatial diffusion of CRs was not included there. This figure suggests that the evolution of the CRP density should be very different from that of the thermal components and disfavors the so-called isobaric model for the CRP distribution. To study that point in more detail, we need a more detailed calculation that can simulate both the cosmological evolution of the cluster and the injection of primary CRs during the evolution. The radial profiles of CR injection obtained in this study should provide some hints for such studies. As we have mentioned in Section 3.2, if the ratio between the turbulent energy and thermal energy increases with radius, the CRP distribution can be more concentrated toward the center (e.g., Pinzke et al. 2017).

Adam et al. (2021) claimed the detection of diffuse gamma-ray emission from the Coma cluster and constrained the CRP energy density. They defined $X_{\rm CRp} = U_{\rm CRp}/U_{\rm th}$, where $U_{\rm CRp}$ and $U_{\rm th}$ are the energy densities enclosed within r_{500} for CRPs and the thermal gas, respectively. Their best-fit value from Fermi data is $X_{\rm CRp} \approx 1\%$, while our secondary-dominant model shown in Figure 9 predicts $X_{\rm CRp} = 6\%$. However, the expected gamma-ray flux below 10 GeV is comparable to the data of the possible detection (Adam et al. 2021; see also Section 4.2.1). The smaller $X_{\rm CRp}$ in their analysis would be due to the steeper spectral indices of $\alpha = 2.6$–2.8. That said, in our primary-dominant model, $X_{\rm CRp} = 0.2\%$ and the gamma-ray flux is one order of magnitude smaller than the possible detection.

3.4. Kolmogorov-type Acceleration

In this section, we show the results for the Kolmogorov-type reacceleration, $q = 5/3$. In this case, the acceleration time becomes shorter for lower-energy CRs: $t_{\rm acc} \propto E^{-1/3}$. As shown in Figure 10, the energy distributions of CRs are fairly different from the hard-sphere case. The maximum energy of CRPs does not increase with reacceleration since $t_{\rm acc}$ above $E_{\rm p}^{\rm max}$ is longer than the calculation time ($\sim$Gyr). All of the low-energy CREs with $E \leqslant$ GeV have $t_{\rm acc}$ shorter than the cooling timescale, so they are efficiently reaccelerated (Figure 1). This makes a bump around GeV in the CRE spectrum sharper than for the hard-sphere case (Figure 6). The bump may be tested by dedicated higher-frequency observations.

Notably, the radio spectrum can be reproduced with reasonable values of ($\tau_{\rm acc}$, $t_{\rm R}$) even in the secondary-dominant models ($f_{\rm ep} = 0$). As with the hard-sphere case, the radio spectra before reacceleration are too hard when $f_{\rm ep} = 0$ (Figure 11, left). However, Kolmogorov reacceleration efficiently accelerates low-energy CREs and the shape of the observed spectrum can be reproduced well. Unlike the hard-sphere case, we use $\tau_{\rm acc} = 100$ Myr, because the reacceleration with $\tau_{\rm acc} \geqslant 200$ Myr causes too sharp bumps in CRE spectra and the resulting synchrotron spectrum does not match the data well. Since $t_{\rm acc}$ for radio-emitting CREs is shorter than that of gamma-emitting CRPs in this case, the increase of $L_{\rm radio}/L_\gamma$ due to reacceleration is larger than for the hard-sphere case. As a result, the Fermi-LAT upper limit is not yet sufficient to give a meaningful constraint on $t_{\rm R}$, except for a soft injection with $\alpha = 2.45$.

We find that the duration of the reacceleration needs to be $t_{\rm R} \approx 180$ Myr to reproduce the convexity in the radio spectrum. The acceleration timescale $t_{\rm acc}$ for CRPs above 10 PeV is longer than 1 Gyr, so there is not so much difference between the "loud" and "quiet" states regarding the PeV neutrino flux (Figure 11). The CR injection power is close to the hard-sphere

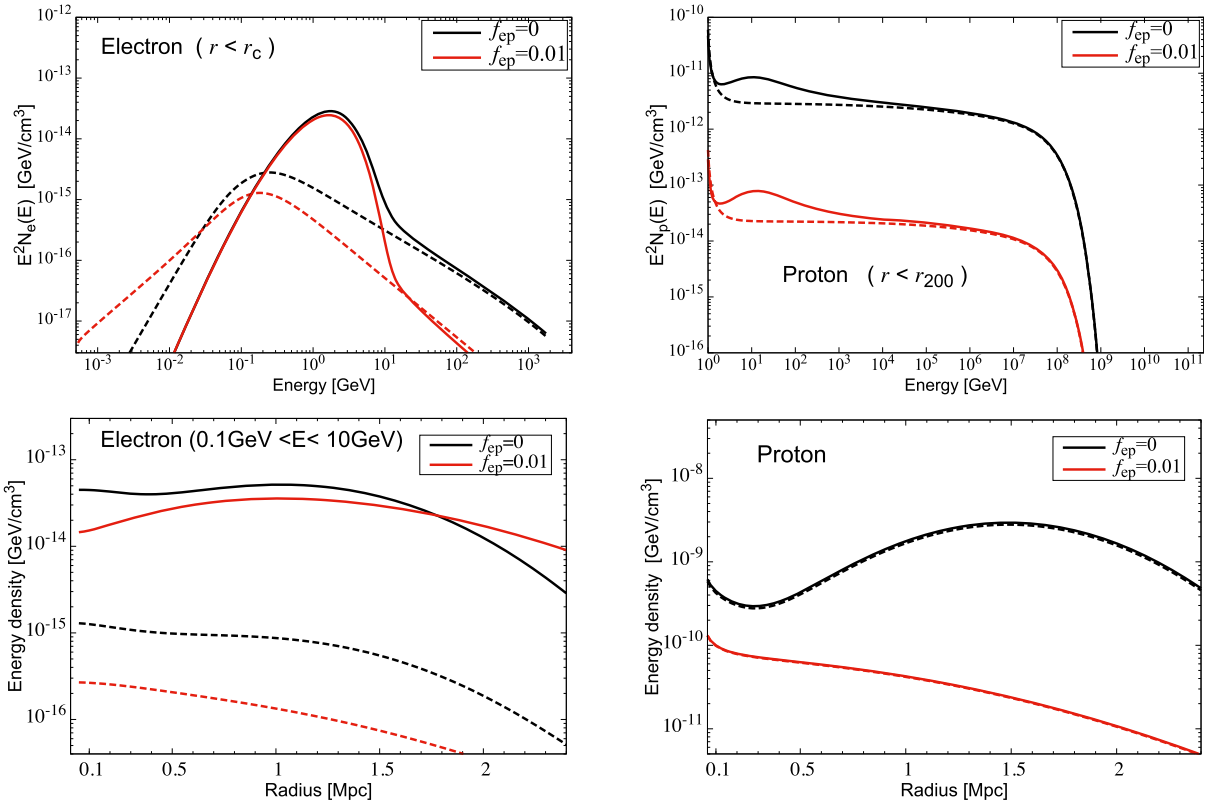

Figure 10. Same as Figure 6, but for the Kolmogorov models with $\tau_{\rm acc} = 100$ Myr. Timescales $t_{\rm R} = 180$ Myr and $t_{\rm R} = 240$ Myr are chosen for $f_{\rm ep} = 0$ and $f_{\rm ep} = 0.01$, respectively (see Table 5).

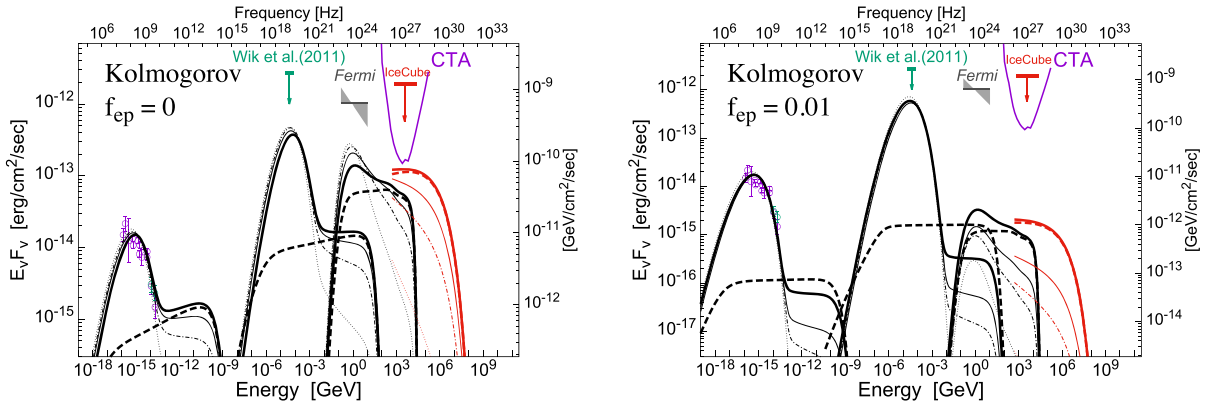

Figure 11. Same as Figure 7, but for the Kolmogorov reacceleration models ($q = 5/3$). Thick lines are the results for $\alpha = 2.0$. The results are reported for $f_{\rm ep} = 0$ (left) and $f_{\rm ep} = 0.01$ (right).

case (Table 2), so the quiet-state fluxes are similar for both reacceleration models.

The predicted neutrino fluxes are mostly determined by the injection index α (Table 5) and the maximum energy, $E_{\rm p}^{\rm max}$. Note that the cutoff shape appears in the neutrino spectrum above 100 TeV directly reflects the cutoff in the primary injection (see Equation (18)). When $E_p^{\rm max} = 10$ PeV, the PeV neutrino flux becomes smaller by a factor of 2.

Our most pessimistic result is obtained when $f_{\rm ep} = 0.01$ (Figure 11, right). That model predicts the fluxes of hadronic radiation more than two orders of magnitude below the IceCube limit. Currently, we cannot exclude those pessimistic scenarios from the radio observations.

3.5. Escaping Cosmic Rays

We can calculate the number flux of CRs that diffuse out from the cluster with the diffusion coefficient D_{rr} and the gradient of particle number density at the boundary of the cluster,

$$\frac{dN_{\rm CR}}{dEdSdt} = -D_{rr}\frac{dn_{\rm p}}{dr}\bigg|_{r=r_{200}}. \quad (36)$$

In Figure 12, we show the energy fluxes of CRPs that escaped from the Coma cluster for different reacceleration models with $\alpha = 2.0$. We can see a clear difference between the two types of reacceleration. The hard-sphere type can accelerate CRPs up to

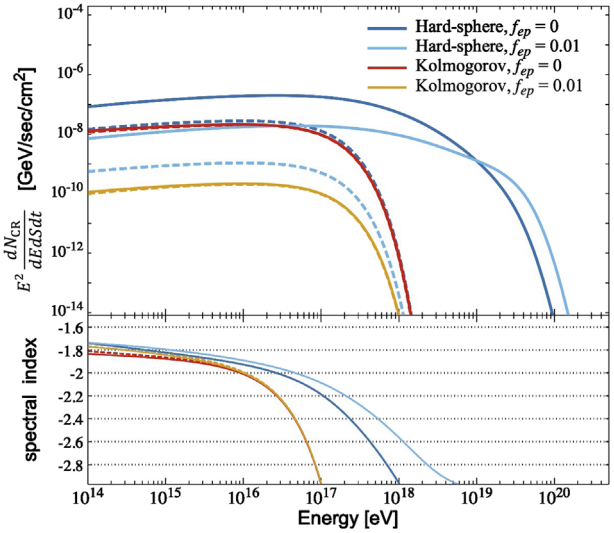

Figure 12. Spectra of CRPs escaping from the virial radius r_{200} of the Coma cluster in the radio-loud state. We show with different colors the results for hard-sphere acceleration ($q=2$) with $f_{\rm ep}=0$ (blue) and $f_{\rm ep}=0.01$ (light blue), and the Kolmogorov acceleration ($q=5/3$) with $f_{\rm ep}=0$ (red) and $f_{\rm ep}=0.01$ (orange). In each model, the injection spectral index is $\alpha=2.0$. Bottom panel shows the spectral indices of the number fluxes in the unit of GeV cm^{-2} s^{-1} (Equation (36)). Spectra for the "loud" and "quiet" states are shown with solid and dashed lines, respectively. The maximum energy of the primary CRPs is assumed to be $E_{\rm p}^{\rm max}=100$ PeV.

ultra-high energies, while the Kolmogorov type never produces CRPs of energies higher than $E_{\rm p}^{\rm max}$.

Note that the fluxes before reacceleration, i.e., at $t=t_0$, differ in each model (dashed lines in the figure). That is simply because we take different injection rates of primary CRs for each model to reproduce the RH in the radio-loud state. In other words, we take different $t_{\rm R}/\tau_{\rm acc}$ for each model, which regulates the energy injection from the turbulent reacceleration. The normalization of the CR injection depends on the choice of $t_{\rm R}$, as smaller $t_{\rm R}/\tau_{\rm acc}$ results in a larger injection power of primary CRs, i.e., a larger flux of escaping CRs.

The maximum energy of CRPs increases with $t_{\rm R}/\tau_{\rm acc}$. In the hard-sphere case, that can be expressed as

$$E_{\rm p}^{\rm max}(t_{\rm R})=E_{\rm p}^{\rm max}(0)\exp\left(\frac{t_{\rm R}}{\tau_{\rm acc}}\right), \quad (37)$$

where $E_{\rm p}^{\rm max}(0)$ is the maximum energy before the reacceleration. When $E_{\rm p}^{\rm max}(0)=100$ PeV, the maximum energy could reach ultra-high energies ($>10^{18.5}$ eV) in $t_{\rm R}/\tau_{\rm acc}=3.44$ or $t_{\rm R}=895$ Myr for $\tau_{\rm acc}=260$ Myr. All values of $t_{\rm R}$ in our calculation are smaller than that value (Table 4). Thus, our model is not sensitive to the parameter $E_{\rm c}^{\rm max}(r)$ in Equation (24), unless $l_{\rm c}^{\rm F}\ll 0.1$ Mpc. Assuming $n_{\rm GC}\sim 10^{-6}$ Mpc^3 for the local number density of galaxy clusters, our model would not overproduce the observed UHECR intensity significantly.

The spectral index of the escaping CRPs is also shown in Figure 12. It becomes harder than the injection index α for $E_{\rm p}\lesssim 10^{16}$–$10^{17}$ eV, which means CRPs below that energy are well confined within the cluster.

4. Discussion

4.1. Caveats

In this section, we discuss various limitations in our assumptions and their potential impacts on our conclusions. We have neglected the uncertainties in the strength and profile of the magnetic field. The constraints on (B_0, η_B) from the RM measurement (Bonafede et al. 2010) are not very stringent, ranging from (B_0, η_B) = (3.0 μG, 0.2) to (7.0 μG, 1.0) within 3σ. In addition, Johnson et al. (2020) pointed out that the magnetic field estimated with RM can include an irreducible uncertain factor of $\sim$3. However, the nondetection of IC radiation provides the lower limit (>0.25 μG) of the magnetic field (Wik et al. 2011).

As reported in Brunetti et al. (2017), the ratio of the radio flux to gamma-ray and neutrino fluxes becomes larger for flatter profiles of the magnetic field, i.e., $\eta_B<0.5$. For example, when $\eta_B=0.2$ and other parameters including B_0 are unchanged, the predicted fluxes of gamma-ray and neutrinos decrease by a factor of $\sim$2. This means that the constraint on $t_{\rm R}/\tau_{\rm acc}$ from the gamma-ray upper limit becomes less stringent; $t_{\rm R}>200$ Myr for the secondary-dominant hard-sphere model with $\tau_{\rm acc}=260$ Myr (see also Figure 3). The injection profile of primary CRs $K(r)$ also depends on the magnetic field profile, as smaller η_B requires a more centrally concentrated $K(r)$. However, in the secondary-dominant scenario, we have confirmed that D_{rr} of Equation (22) requires an injection profile with a peak at $r\geqslant 0.8$ Mpc even in the extreme case of a uniform magnetic field ($\eta_B=0$).

Although we have fixed D_{rr} as Equation (22), smaller values of D_{rr} could be possible, depending on the turbulent nature of the ICM. The radial diffusion of parent CRPs is one of the causes of the hard synchrotron spectrum in the secondary-dominant model (Figure 7). For $\alpha=2.45$, we confirmed that the RH spectrum actually fits well when D_{rr} is 1/10 times smaller than Equation (22). The spectral hardening due to the energy dependence in the pp cross section is unavoidable even for $D_{rr}\equiv 0$, which makes it difficult to fit the RH spectrum with harder injections ($\alpha\leqslant 2.2$) in the hard-sphere model. A smaller $\tau_{\rm acc}$ would result in a better match at higher frequencies around $\sim$1 GHz, but would worsen the fit at lower frequencies around $\sim$20 MHz. Note that the Kolmogorov model does not have to suffer from the difficulty due to hard indices (Figure 11).

We have also assumed that $f_{\rm ep}$ and D_{pp} are constant with radius. Under this condition, we showed that the profile of the RH can be reproduced by the stable injection profile shown in Figure 5 combined with the spatial diffusion of CRPs. However, the secondary-dominant model results in the hardening in the radio spectrum (Figure 7). That said, some numerical simulations suggest that the ratio of turbulent pressure to the thermal one increases with distance from the cluster center (e.g., Nelson et al. 2014; Vazza et al. 2018). Pinzke et al. (2017) showed that the profile of the RH can also be reproduced when the efficiency of reacceleration with radius and the CR distribution is more concentrated toward the central region. In such models, the tension in the RH spectrum would be partially relaxed.

In our calculation, the time dependence of some quantities, such as $n_{\rm th}(r)$, $B(r)$, $f_{\rm ep}$, and $Q_{\rm p}$, is not taken into account. The statistical properties of RHs would give constraints on the time evolution of those quantities, which should be studied in future studies.

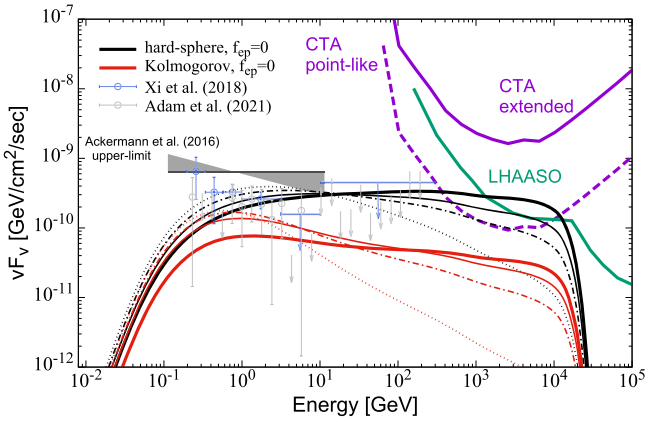

Figure 13. Expected gamma-ray fluxes. As a reference, we show the spectra of the possible extended component of the gamma-ray source obtained by Xi et al. (2018; radio+p1 model, blue points) and Adam et al. (2021; scenario 3 extended model, gray points). The arrows show the upper limits. The magenta and green lines show the point-source sensitivity of CTA North (50 hr) and LHAASO (five years), respectively. The dashed magenta line shows the CTA sensitivity for extended sources with a subtended angle of $1.^{\circ}2$ (see text). The black and red lines are the fluxes for the radio-loud state. In each model, we assume the secondary-dominant model ($f_{\rm ep} = 0$). The results for four different injection indices $\alpha = 2.0$, 2.1, 2.2, and 2.45 (thick solid, thin solid, thin dotted–dashed, thin dotted) are shown.

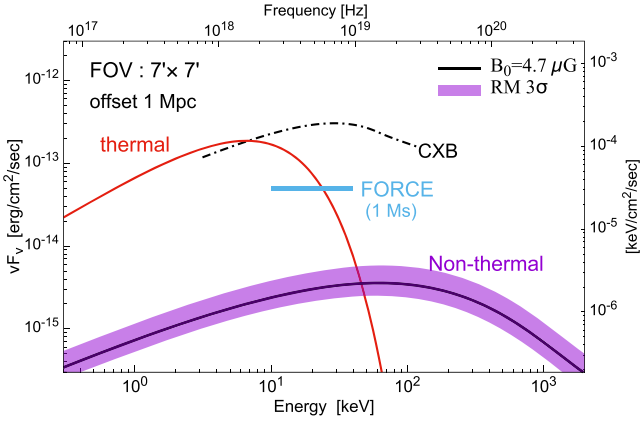

Figure 14. Expected hard X-ray fluxes. Free–free emission from the thermal ICM electron is shown in red, and ICS radiation from CREs is shown with the solid black line. The shaded region corresponds to the 3σ uncertainty in the magnetic field B_0 measured by Bonafede et al. (2010). Intensities of that emission are integrated within the $7' \times 7'$ region, which corresponds to the FOV of FORCE. Note that the center of the FOV is shifted by 1 Mpc ($\approx 36'$) from the cluster center. The black dotted–dashed line shows the cosmic X-ray background (CXB), which is evaluated from the CXB intensity measured with INTEGRAL (Churazov et al. 2007). As a reference, the target sensitivity of FORCE for point-like sources is shown with the thick cyan line.

4.2. Future Prospects for Detecting High-energy Emission

4.2.1. Gamma-Rays

Observations of gamma-ray photons from the ICM provide important constraints on the amount of CRPs. In this paper, we have adopted the upper limit given by Ackermann et al. (2016a), taking a conservative approach. However, there are three recent studies that claimed a possible detection in the direction of the Coma cluster using Fermi data (Keshet & Reiss 2017; Xi et al. 2018; Abdollahi et al. 2020; Ballet et al. 2020; Adam et al. 2021). Although a point source (4FGL J1256.9+2736) may account for most of the signal, Adam et al. (2021) showed that models including extended components match the data better.

In Figure 13, we plot the gamma-ray spectrum given by Xi et al. (2018; blue points) and Adam et al. (2021; gray points). Here, we have assumed $r_{\rm ap} = 2.0$ Mpc to calculate the expected fluxes, the same as in Figure 7. Our secondary-dominant models are in good agreement with the data at around a ∼GeV, except for the Kolmogorov model with $\alpha = 2.0$, where the relatively large value of $t_{\rm R}$ results in small values of $F_\gamma/F_{\rm radio}$ (Section 3.2). It is worth noting that the upper limit given by Xi et al. (2018) in [3, 10] GeV is incompatible with our secondary-dominant hard-sphere models (black lines) with $\alpha \leqslant 2.45$. However, Adam et al. (2021) obtained different constraints in the same energy range, and the deep limit obtained by Xi et al. (2018) is still controversial. Future observations or analysis around this energy range are necessary to give robust constraints on the reacceleration, primary CREs, and the injection indices.

We also show the sensitivities of the future TeV gamma-ray telescopes: the Cherenkov Telescope Array (CTA) and Large High Altitude Air Shower Observatory (LHAASO). The dashed magenta line shows the point-source sensitivity of the CTA North site with 50 hr of observation. With this sensitivity, TeV gamma-rays from the Coma cluster can be accessible only for the optimistic hard-sphere model with $f_{\rm ep} = 0$. The flux becomes $\sim 1/10$ in the primary-dominant scenario ($f_{\rm ep} = 0.01$; see Figure 8).

Since the RH of Coma is an extended source for CTA, its sensitivity should be modified for its extension. The angular resolution of the instrument at 1 TeV is $\theta_{\rm inst} \approx 4'$, while the subtended angle corresponding to the radius of $r = 2.0$ Mpc is $\theta_{\rm source} \approx 1.^{\circ}2$. We estimate the flux sensitivity for an extended source by multiplying the point-source sensitivity by the factor $\max[1, \theta_{\rm inst}/\theta_{\rm source}]$ (solid magenta), assuming that the sensitivity is limited by the background. We here implicitly assumed an ON/OFF analysis and constant intensity over the observed extension, although these assumptions may not be optimal for instruments with better sensitivities. We caution that the diffuse sensitivity estimated here should be regarded as an upper limit. However, the angular resolution of LHAASO is $\sim 1^{\circ}$ (Bai et al. 2019), so that the Coma cluster can be approximated as a point source (solid green). It seems challenging to detect extended gamma-ray emission from the Coma cluster with CTA, but the point-like signal can be accessible with LHAASO.

4.2.2. Hard X-Ray

In our calculation, the distribution of CREs in the radio-loud state is constrained by the RH observation, so the ICS flux is almost uniquely determined for a given magnetic field. Figure 14 shows spectra of X-ray emission from both thermal and nonthermal components in the ICM, which are integrated within the field of view (FOV) of the future X-ray mission Focusing On Relativistic universe and Cosmic Evolution (FORCE). The free–free emission is calculated with the profiles of temperature and density shown in Equations (3) and (4). The center of the FOV is shifted by 1 Mpc from the cluster center, where the thermal X-ray flux is too bright. Since the flat distribution of CREs up to $r \approx 1$ Mpc is more extended than the ICM or the magnetic field, the relative strength of the no-thermal flux to the thermal X-ray increases up to this radius. In our calculation, where Equation (20) with $B_0 = 4.7\,\mu$G is adopted for the magnetic field, the predicted ICS flux is $F_{\rm X} \approx 2.0 \times 10^{-15}\,{\rm erg\,cm^{-2}\,s^{-1}}$ at 30 keV, which is smaller

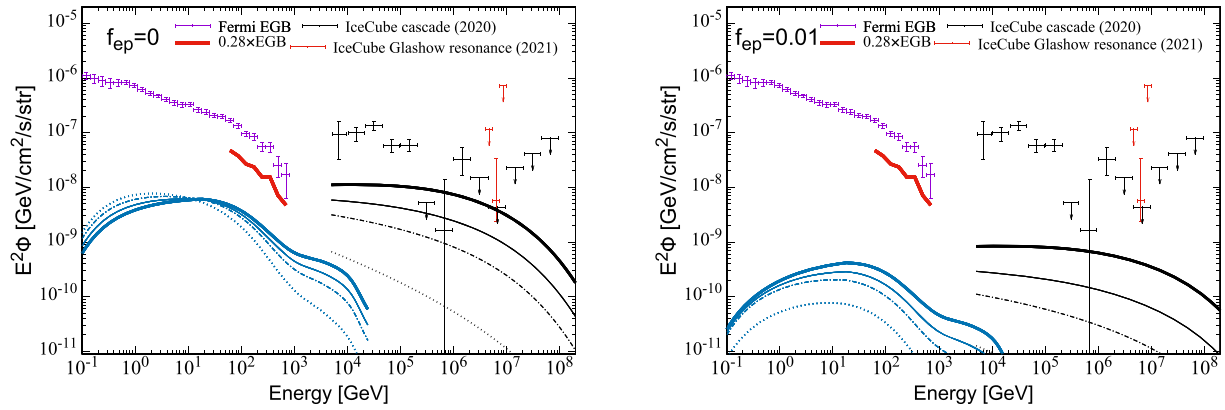

Figure 15. Background intensities of gamma-rays (blue) and neutrinos (black) for hard-sphere models ($q = 2$). The magenta data points are the total EGB intensity observed with Fermi (Ackermann et al. 2015). As a reference, we show the EGB intensity multiplied by 0.28 with thick red line above 50 GeV, which corresponds to the approximate upper limit for the contribution from nonblazar components. The black crosses show the all-flavor neutrino intensity of the IceCube cascade events (Aartsen et al. 2020b), while the red ones show the data at the energy of the Glashow resonance (IceCube Collaboration et al. 2021). We adopt the effective optical depth for the EBL attenuation consistent with $\xi_z = 1$. Left: results for the secondary-dominant models ($f_{ep} = 0$). Right: results for the primary-dominant models ($f_{ep} = 0.01$). The results for four different injection indexes are shown: $\alpha = 2.0$, 2.1, 2.2, and 2.45 (thick solid, thin solid, thin dotted–dashed, thin dotted).

than the thermal flux by almost two orders of magnitude below 10 keV. The nonthermal flux becomes comparable to the thermal one only above ∼50 keV, though it is still significantly smaller than the cosmic X-ray background (CXB, black dotted–dashed).

The hard X-ray satellite FORCE is characterized by its high sensitivity and high angular resolution in a broad band of 10–80 keV (Mori et al. 2016). Thanks to its high angular resolution of 15″ and the target sensitivity within 1 Ms of $S_X = 3 \times 10^{-15}$ erg cm^{-2} s^{-1} keV^{-1} for point-like sources, FORCE is expected to resolve ∼80% of the CXB emission into point sources (Nakazawa et al. 2018), which can reduce the background flux by a factor of ∼3. We expect the very first detection of the ICS emission from high-redshift RHs or radio relics is expected with this instrument. Several MeV gamma-ray missions, such as the Compton Spectrometer and Imager (COSI), Gamma-Ray and AntiMatter Survey (GRAMS), and All-sky Medium Energy Gamma-ray Observatory (AMEGO), are being planned (Tomsick et al. 2019; McEnery et al. 2019; Aramaki et al. 2020). Those instruments will constrain the ICS components from clusters above ∼100 keV energies.

4.3. Contributions to Cumulative Neutrino and Gamma-Ray Backgrounds

Once the luminosity of high-energy emission and the number density of the sources are specified, we can evaluate the intensity of the background emission. The cumulative background intensity is estimated by (e.g., Waxman & Bahcall 1999)

$$E^2\Phi \approx \frac{c}{4\pi} E \frac{dQ}{dE} \xi_z t_H, \tag{38}$$

where the Hubble time is $t_H \approx 13$ Gyr, and $\xi_z \sim \mathcal{O}(1)$ is a parameter that depends on the redshift evolution of the luminosity density Q. For example, $\xi_z \sim 3.0$ for the evolution of the star formation rate, i.e., $n_s \propto (1+z)^m$ with $m = 3$, while $\xi_z \approx 0.6$ for nonevolving sources ($m = 0$). Here, we take $\xi_z = 1$ as a reference value. Note that ξ_z is reduced only by a factor of 2−3 even for negatively evolving ($m < 0$) sources. The generation rate density of gamma-ray photons or high-energy neutrinos per unit comoving volume $dQ/d\ln E = E(dQ/dE)$ is evaluated from

$$E\frac{dQ}{dE} \approx n_{GC}^{eff} E^2 \frac{d\dot{N}}{dE}\bigg|_{Coma}, \tag{39}$$

where $\frac{d\dot{N}}{dE}\big|_{Coma}$ is the luminosity of hadronic emission from the Coma cluster at the radio-loud state, and the effective number density of the radio-loud clusters n_{GC}^{eff} is the product of the observed radio-loud fraction $f_{loud} \approx 0.4$ (Kale et al. 2013; Cassano et al. 2016) and the number density of Coma-like clusters with the virial mass of $M_{500} \approx 6 \times 10^{14}\ h^{-1} M_\odot$ (Reiprich & Bohringer 2002), $n_{GC} \sim 10^{-6}$ Mpc^{-3} (e.g., Jenkins et al. 2001). The virial mass M_Δ is defined as $M_\Delta = 4\pi r_\Delta^3 \rho_m/3$ and ρ_m is the mean matter density of the universe.

In Figure 15, we show high-energy neutrino and gamma-ray background intensities from Coma-like clusters estimated from Equation (38). Following Murase et al. (2012), we estimate the effective optical depth for the EBL attenuation consistent with $\xi_z = 1$. Note that the mass function of the dark matter halo is quite sensitive to the mass around M $\sim 10^{15}\ h^{-1} M_\odot$. Our treatment of n_{GC} is so rough that the estimate of the background intensities includes the ambiguity of a factor of 2−5.

According to Ackermann et al. (2016b), about 70% of the extragalactic gamma-ray background (EGB) above 50 GeV is likely to originate from resolved and unresolved point sources like blazars, so the gamma-ray background from clusters would be smaller than ∼30% of the observed EGB intensity (see also Lisanti et al. 2016). The red line in Figure 15 shows the 1σ upper limit for the nonblazar component (Ackermann et al. 2016b). The gamma-ray backgrounds of both secondary-dominant and primary-dominant models are well below this limit even when the ambiguity in our estimate is taken into account.

We see that the neutrino intensity for the secondary-dominant model with $\alpha = 2.0$ (left panel, thin solid) becomes $\lesssim$3%–30% of the observed one, which is consistent with previous results on the typical accretion shock scenario (Murase et al. 2008; Fang & Olinto 2016; Hussain et al. 2021). Note that the neutrino luminosity function has not

been considered in our estimate. By including the cluster mass function and its redshift evolution as well as the CR distribution, the intensities can be further enhanced by a factor of $\sim\mathcal{O}(1)-\mathcal{O}(10)$, in which $\sim$100% of the IceCube intensity can be explained. For example, if CRPs are mainly injected from internal sources like AGNs, the redshift evolution of the source density can be as large as $\xi_z\sim 3$, instead of $\xi_z\sim 1$ (e.g., Fang & Murase 2018; Hussain et al. 2021). The neutrino luminosity scales with $L_\nu\propto M_{500}$ (that is different from the accretion shock scenario); the background intensity mainly originates from more clusters lighter than Coma (Murase et al. 2013). Such a contribution is not constrained by current radio observations (Zandanel et al. 2015), and larger effective number densities are consistent with the present IceCube limit from multiplet searches (Murase & Waxman 2016). However, the contribution to the IceCube neutrino intensity can be as much as $\sim$3% in the primary-dominant model, and we caution there are many uncertainties in the estimate.

Here, we note an important constraint that is applied when the injected CR luminosity density is normalized by the IceCube data. In this case, softer spectral indexes with $\alpha\gtrsim 2.2$ are excluded, because such models inevitably overproduce the gamma-ray background around 10–100 GeV (Murase et al. 2013). However, in our calculation, the normalization is given by the radio luminosity, and their contribution to the EGB is minor. This result (see Figure 15) is also consistent with previous work (Murase et al. 2009). The intensity of such cosmogenic gamma-rays, which is not shown in Figure 15, is compatible with the nonblazar EGB. The contribution of gamma-rays from clusters can be only $\sim$1%–10% of the IGRB and smaller, especially in the central source scenario if CRs are confined inside radio lobes.

4.4. Comparison with Previous Studies

There are several studies that calculated the cumulative neutrino intensity. Murase et al. (2008) calculated the neutrino background by convolving the neutrino luminosity with the mass function of dark matter halos assuming that galaxy clusters are the sources of CRs above the second knee, and predicted that the all-sky neutrino intensity is $E_\nu^2\Phi_\nu\sim(0.3\text{–}3)\times 10^{-8}$ GeV cm^{-2} s^{-1} sr^{-1} for $\alpha=2.0$, considering both accretion shock and AGN scenarios (Murase 2017). A similar neutrino intensity was found by Kotera et al. (2009) who assumed an AGN as a central source. Murase et al. (2013) showed that these models are viable for the IceCube data if the CR spectrum is hard and low-mass clusters are dominant, and steep CR spectra lead to negligible contributions (Ha et al. 2020). Fang & Olinto (2016) estimated the contribution to the IceCube intensity from galaxy clusters, taking into account the 1D spatial diffusion of CRPs. They adopted the CRP injection luminosity similar to our secondary-dominant models ($L_{\rm p}^{\rm inj}\sim 10^{45}$ erg s^{-1}) and concluded that the accretion shock scenario could explain only $\lesssim$20%, while the central source scenario could explain both the flux and spectrum of the IceCube data above $\sim$100 TeV.

Including the radio constraints, Zandanel et al. (2015) evaluated the gamma-ray and neutrino background with both phenomenological and semi-analytical approaches. They obtained the maximum neutrino fluxes for nearby clusters at 250 TeV assuming a simple relation between the gamma-ray luminosity and cluster mass:

$$\log_{10}\left[\frac{L_\gamma(100\ {\rm MeV})}{{\rm s}^{-1}\,{\rm GeV}^{-1}}\right]=P_1+P_2\log_{10}\left(\frac{M_{500}}{M_\odot}\right), \tag{40}$$

where $P_1\approx 20$ is determined so that the cumulative number of radio-loud cluster counts does not overshoot the observed counts from National Radio Astronomy Observatory Very Large Array sky survey (NVSS), which is found in, e.g., Cassano et al. (2010). They fixed $P_2=5/3$ assuming that the luminosity of hadronic emission scales as the cluster thermal energy, i.e., $L_\gamma\propto M_{500}^{5/3}$ according to the accretion shock scenario. They also assumed that the radio luminosity $L_{\rm radio}$ linearly scales with L_γ, so they implicitly assumed $L_{\rm radio}\propto M_{500}^{5/3}$. Their models with the magnetic field of $B=1\ \mu$G typically predicted the gamma-ray flux from Coma-like clusters to be $F_\gamma\sim 10^{-10}$ GeV cm^{-2} s^{-1} at 100 MeV, which is similar to our results in the secondary-dominant models. They concluded that the contribution to the IceCube flux from all clusters is at most 10% in their phenomenological modeling, which is in line with our results in Section 4.3. That said, these radio constraints are much weaker for the central source scenario, where lower-mass and higher-redshift sources are important as discussed above. Along this line, Fang & Murase (2018) investigated the AGN scenario, in which the all-sky UHECR, neutrino, and nonblazar EGB fluxes are explained simultaneously, and a similar flux level is obtained by Hussain et al. (2021).

5. Conclusions

In this paper, we have studied the CR distribution in the giant RH of the Coma cluster. Our model includes most of the physical processes concerning CRs in galaxy clusters: turbulent reacceleration, injection of both primary and secondary CREs, and diffusion of parent CRPs. We have followed the turbulent reacceleration scenario (e.g., Schlickeiser et al. 1987) and modeled the multiwavelength and neutrino emission from the RH by solving the one-dimensional FP equations (Equations (1) and (5)) numerically.

We have modeled the spatial evolution of the CRs with the diffusion approximation (Equation (22)) and nonuniform injections (Equations (34) and (35)). Secondary CREs are injected through inelastic *pp* collisions (Equation (11)). A merging activity of the cluster suddenly turns on the reacceleration (Equation (24)), and CREs are reaccelerated up to $\sim$1 GeV to form the RH. CRPs are also reaccelerated and power the associated emission of gamma-rays and neutrinos (Equations (27)–(29)). We have assumed a radial dependence of the magnetic field (Equation (20)) and ICM density (Equation (3)), and adopted the best-fit parameters from a RM measurement (Bonafede et al. 2010).

The detailed nature of turbulence is still unknown. We have examined two types of reacceleration: the hard-sphere type ($q=2$) and the Kolmogorov type ($q=5/3$). We adopted $\tau_{\rm acc}=260$ Myr and $\tau_{\rm acc}=100$ Myr for $q=2$ and $q=5/3$, respectively. We have tested two extreme cases for the amount of primary CREs: the secondary-dominant model ($f_{\rm ep}=0$) and the primary-dominant model ($f_{\rm ep}=0.01$). The observed radio spectrum and the gamma-ray upper limit give constraints on the duration of the reacceleration t_R. The radial dependence of the

injection $K(r)$ is constrained by the surface brightness profile of the RH. Note that those quantities are constrained under the assumption that $\tau_{\rm acc}$ and $f_{\rm ep}$ are constant with radius.

The main results of this work are summarized below:

1. The secondary-dominant models ($f_{\rm ep}=0$) with hard-sphere reacceleration ($q=2$) produce hard synchrotron spectra compared to the observations even for $\alpha=2.45$ (Figure 7). That hardness is caused by the energy-dependent diffusion of parent CRPs together with the weak energy dependence in the *pp* cross section.
2. The CRE distribution is required to be nearly uniform within the RH under the assumption that the reacceleration timescale does not depend on the radius. That requirement disfavors centrally concentrated injections, such as the delta-functional injection from the center.
3. The required injection profiles of primary CRs significantly differ between the secondary-dominant and primary-dominant models. The injection should occur at the edge of the RH in the former case, while the injection itself needs to be uniform in the latter case.
4. The radio spectrum can be reproduced in both hard-sphere and Kolmogorov models by adjusting the value of $t_{\rm R}/\tau_{\rm acc}$. The Kolmogorov models are more compatible with the secondary-dominant scenario.
5. Regarding hadronic emission, the most optimistic results are obtained in the case of the hard-sphere reacceleration ($q=2$). Neutrino and gamma-ray fluxes can optimistically be as large as $\sim 10^{-10}\,{\rm GeV\,cm^{-2}\,s^{-1}}$, and the next generation of TeV gamma-ray telescopes such as LHAASO may detect gamma-rays from the Coma RH.
6. The models with pessimistic assumptions about hadronic emission, such as the primary-dominant scenario ($f_{\rm ep}=0.01$) or the Kolmogorov reacceleration ($q=5/3$) from the radio constraints can also reproduce the observed radio properties.

We discussed the detectability of gamma-rays and hard X-rays with future experiments in Section 4.2. As seen in Figure 14, hard X-ray emission is dominated by free–free emission from thermal electrons below $\sim$50 keV. The deviation from the thermal spectrum is pronounced only above $\sim$50 keV, so new instruments with better sensitivities in the 10–100 keV band are necessary.

We have estimated high-energy neutrino and gamma-ray backgrounds from Coma-like clusters. Notably, we have taken into account effects of CRP and CRE reacceleration such that the models are consistent with the radio observations of Coma. Our estimate suggests that the contribution from the radio-loud massive galaxy clusters in the local universe is $\lesssim$3%–30% of the observed neutrino intensity, which is consistent with previous results (e.g., Fang & Olinto 2016; Murase & Waxman 2016; Hussain et al. 2021), although a larger contribution may come from lower-mass/higher-redshift clusters.

The authors thank the anonymous referee for the useful comments that greatly improved the presentation of the paper. K.N. acknowledges the support by the Forefront Physics and Mathematics Program to Drive Transformation (FoPM). Numerical computations were in part carried out on Cray XC50 at the Center for Computational Astrophysics, National Astronomical Observatory of Japan. This work is supported by the joint research program of the Institute for Cosmic Ray Research (ICRR), the University of Tokyo. The work of K.M. is supported by NSF grant No. AST-1908689, and KAKENHI No. 20H01901 and No. 20H05852.

Appendix A
Inverse-Compton Radiation

In this paper, we adopt the formula for the inverse-Compton radiation given in Inoue & Takahara (1996), which is accurate enough in both the Thomson and Klein–Nishina regimes. The energies of soft (i.e., CMB) photons, scattered photons, and CREs are denoted as $\epsilon_0 m_{\rm e}c^2$, $\epsilon m_{\rm e}c^2$, and $\gamma m_{\rm e}c^2$, respectively. The photon production rate can be expressed as

$$q(r,\,\epsilon)=\int d\epsilon_0 n(\epsilon_0)\int d\gamma n_{\rm e}(r,\,\gamma)C(\epsilon,\,\gamma,\,\epsilon_0), \tag{A1}$$

where $n_0(\epsilon_0)$ is the number density of CMB photons per $d\epsilon_0$, which is equivalent to that of blackbody radiation with temperature $T=T_0(1+z)$:

$$n_0(\epsilon_0)=\frac{8\pi}{c^3}\left(\frac{m_{\rm e}c^2}{h}\right)^3\frac{\epsilon_0^2}{\exp(\frac{\epsilon_0 m_{\rm e}c^2}{k_B T})-1}, \tag{A2}$$

where $T_0=2.757$ K, and $z=0.0232$ is the redshift of Coma cluster. The function C in Equation (A1) is called the Compton kernel, which is (see Jones 1968)

$$C(\epsilon,\,\gamma,\,\epsilon_0)=\frac{2\pi r_{\rm e}^2 c}{\gamma^2\epsilon_0}\left[2\kappa\ln\kappa+(1+2\kappa)(1-\kappa)+\frac{(4\epsilon_0\gamma\kappa)^2}{2(1+4\epsilon_0\gamma\kappa)}(1-\kappa)\right], \tag{A3}$$

where $\kappa=\frac{\epsilon}{4\epsilon_0\gamma(\gamma-\epsilon)}$. The emission coefficient can be written as

$$\varepsilon_\nu^{\rm IC}(\nu,\,r)=\frac{h}{4\pi}\epsilon\, q(r,\,\epsilon),\ \nu=\frac{m_{\rm e}c^2}{h}\epsilon. \tag{A4}$$

Also, the momentum loss rate used in Equation (5) is written as

$$b_{\rm IC}(\gamma)=\int d\epsilon_0\int d\epsilon\,(\epsilon m_{\rm e}c^2)n_0(\epsilon_0)C(\epsilon,\,\gamma,\,\epsilon_0). \tag{A5}$$

Appendix B
Pion and Secondary Neutrino Spectra

In this paper, we adopt the approximate expression for the spectra of pions and neutrinos given in Kelner et al. (2006). For pion production (Equation (10)) from the inelastic *pp* collision, we apply their QGSJET model, regardless of the energy of pions. The spectrum of pions produced by the *pp* collision of a CRP of energy $E_{\rm p}$ is approximated as

$$F_\pi(E_\pi,\,E_{\rm p})=4\phi B_\pi x^{\phi-1}\left(\frac{1-x^\phi}{(1+ux^\phi)^3}\right)^4\times\left(\frac{1}{1-x^\phi}+\frac{3u}{1+ux^\phi}\right)\left(1-\frac{m_\pi}{xE_{\rm p}}\right)^{1/2}, \tag{B1}$$

with the best-fit parameters

$$B_\pi=5.58+0.78L+0.10L^2, \tag{B2}$$

$$u = \frac{3.1}{B_\pi^{3/2}},\ \phi = \frac{0.89}{B_\pi^{1/2}(1 - e^{-0.33B_\pi})}, \tag{B3}$$

where $x = E_\pi/E_p$ and $L = \ln(E_p/10^3\,\mathrm{GeV})$. We use this expression for the pion production by all CRPs above the threshold energy $E_{th} \approx 1.32$ GeV.

The neutrino spectra from the decay of charged ultra-relativistic pions are also given in Kelner et al. (2006). The spectra of muonic neutrinos from the decay of secondary muons used in Equation (28) is written as

$$f_{\nu_\mu^{(2)}} = g_{\nu_\mu}(x)\Theta(x - \eta) + (h_{\nu_\mu}^{(1)} + h_{\nu_\mu}^{(2)})\Theta(\eta - x), \tag{B4}$$

where $\eta = 1 - \zeta = (m_\mu/m_\pi)^2 = 0.573$, and

$$g_{\nu_\mu}(x) = \frac{3 - 2\eta}{9(1 - \eta)^2}(9x^2 - 6\ln x - 4x^3 - 5), \tag{B5}$$

$$h_{\nu_\mu}^{(1)}(x) = \frac{3 - 2\eta}{9(1 - \eta)^2}(9\eta^2 - 6\ln\eta - 4\eta^3 - 5), \tag{B6}$$

$$h_{\nu_\mu}^{(2)}(x) = \frac{(1 + 2\eta)(\eta - x)}{9\eta^2}[9(\eta + x) - 4(\eta^2 + \eta x + x^2)]. \tag{B7}$$

Similarly, for electron neutrinos

$$f_{\nu_e} = g_{\nu_\mu}(x)\Theta(x - \eta) + (h_{\nu_e}^{(1)} + h_{\nu_e}^{(2)})\Theta(\eta - x), \tag{B8}$$

where

$$g_{\nu_e}(x) = \frac{2(1 - x)}{3(1 - \eta)^2}\left[6(1 - x)^2 + \eta(5 + 5x - 4x^2) + \frac{6\eta\ln x}{1 - x}\right], \tag{B9}$$

$$h_{\nu_e}^{(1)}(x) = \frac{2}{3(1 - \eta)^2}[(1 - \eta)(6 - 7\eta + 11\eta - 2 - 4\eta^3) + 6\eta\ln\eta], \tag{B10}$$

$$h_{\nu_e}^{(2)}(x) = \frac{2(\eta - x)}{3\eta^2}(7\eta^2 - 4\eta^3 + 7x\eta - 4x\eta^2 - 2x^2 - 4x^2\eta). \tag{B11}$$

Note that a minor typo in Equation (B9) in Kelner et al. (2006) is fixed here.

ORCID iDs

Kosuke Nishiwaki https://orcid.org/0000-0003-2370-0475
Katsuaki Asano https://orcid.org/0000-0001-9064-160X
Kohta Murase https://orcid.org/0000-0002-5358-5642

References

Aartsen, M. G., Abbasi, R., Abdou, Y., et al. 2013, PhRvL, 111, 021103
Aartsen, M. G., Ackermann, M., Adams, J., et al. 2014, ApJ, 796, 109
Aartsen, M. G., Ackermann, M., Adams, J., et al. 2020a, PhRvL, 124, 051103
Aartsen, M. G., Ackermann, M., Adams, J., et al. 2020b, PhRvL, 125, 121104
Abdollahi, S., Acero, F., Ackermann, M., et al. 2020, ApJS, 247, 33
Abell, G. O., Corwin, H. G. J., & Olowin, R. P. 1989, ApJS, 70, 1
Ackermann, M., Ajello, M., Albert, A., et al. 2015, ApJ, 799, 1
Ackermann, M., Ajello, M., Albert, A., et al. 2016a, ApJ, 819, 149
Ackermann, M., Ajello, M., Albert, A., et al. 2016b, PhRvL, 116, 151105
Adam, R., Goksu, H., Brown, S., Rudnick, L., & Ferrari, C. 2021, A&A, 648, A60
Adam, R., Goksu, H., Leingärtner-Goth, A., et al. 2020, A&A, 644, A70
Amano, T., & Hoshino, M. 2008, ApJ, 690, 244
Aramaki, T., Adrian, P. O. H., Karagiorgi, G., & Odaka, H. 2020, APh, 114, 107
Bai, X., Bi, B. Y., Bi, X. J., et al. 2019, arXiv:1905.02773
Ballet, J., Burnett, T. H., Digel, S. W., & Lott, B. 2020, arXiv:2005.11208
Becker, P. A., Le, T., & Dermer, C. D. 2006, ApJ, 647, 539
Berezinsky, V. S., Blasi, P., & Ptuskin, V. S. 1997, ApJ, 487, 529
Blasi, P., & Colafrancesco, S. 1999, APh, 12, 169
Bonafede, A., Feretti, L., Murgia, M., et al. 2010, A&A, 513, 1
Bonamente, M., Lieu, R., & Bulbul, B. 2009, ApJ, 696, 1886
Briel, U. G., Henry, J. P., & Boehringer, H. 1992, A&A, 259, L31
Brown, S., & Rudnick, L. 2011, MNRAS, 412, 2
Brunetti, G., & Blasi, P. 2005, MNRAS, 363, 1173
Brunetti, G., Cassano, R., Dolag, K., & Setti, G. 2009, A&A, 507, 661
Brunetti, G., & Jones, T. W. 2014, IJMPD, 23, 1
Brunetti, G., & Lazarian, A. 2007, MNRAS, 378, 245
Brunetti, G., & Lazarian, A. 2011, MNRAS, 412, 817
Brunetti, G., Rudnick, L., Cassano, R., et al. 2013, A&A, 558, 1
Brunetti, G., Zimmer, S., & Zandanel, F. 2017, MNRAS, 472, 1506
Brunetti, G. 2015, PPCF, 58, 014011
Bykov, A. M., Vazza, F., Kropotina, J. A., Levenfish, K. P., & Paerels, F. B. S. 2019, SSRv, 215, 14
Cassano, R., & Brunetti, G. 2005, MNRAS, 357, 1313
Cassano, R., Brunetti, G., Giocoli, C., & Ettori, S. 2016, A&A, 593, A81
Cassano, R., Ettori, S., Giacintucci, S., et al. 2010, ApJL, 721, 1
Churazov, E., Sunyaev, R., Revnivtsev, M., et al. 2007, A&A, 467, 529
Churazov, E., Vikhlinin, A., Zhuravleva, I., et al. 2012, MNRAS, 421, 1123
Cuciti, V., Cassano, R., Brunetti, G., et al. 2015, A&A, 580, A97
Dennison, B. 1980, ApJL, 239, L93
Dermer, C. D., & Menon, G. 2009, High Energy Radiation from Black Holes: Gamma Rays, Cosmic Rays, and Neutrinos (Princeton, NJ: Princeton Univ. Press)
Domínguez, A., Primack, J. R., Rosario, D. J., et al. 2011, MNRAS, 410, 2556
Ensslin, T. A., Biermann, P. L., Klein, U., & Kohle, S. 1998, A&A, 332, 395
Enßlin, T. A., Biermann, P. L., Kronberg, P. P., & Wu, X.-P. 1997, ApJ, 477, 560
Fang, K., & Murase, K. 2018, NatPh, 14, 396
Fang, K., & Olinto, A. V. 2016, ApJ, 828, 37
Fujita, Y., Ohira, Y., & Yamazaki, R. 2013, ApJL, 767, L4
Fujita, Y., Takizawa, M., & Sarazin, C. L. 2003, ApJ, 584, 190
Gaisser, T. K. 1991, Cosmic Rays and Particle Physics (Cambridge: Cambridge Univ. Press)
Giovannini, G., Feretti, L., Venturi, T., Kim, K. T., & Kronberg, P. P. 1993, ApJ, 406, 399
Goldreich, P., & Sridhar, S. 1995, ApJ, 438, 763
Gould, R. 1972, Phy, 60, 145
Govoni, F., Enßlin, T. A., Feretti, L., & Giovannini, G. 2001, A&A, 369, 441
Ha, J.-H., Ryu, D., & Kang, H. 2020, ApJ, 892, 86
Hussain, S., Alves Batista, R., de Gouveia Dal Pino, E. M., & Dolag, K. 2021, MNRAS, 507, 1762
IceCube Collaboration 2013, Sci, 342, 1242856
IceCube Collaboration, Aartsen, M. G., Abbasi, R., Ackermann, M., et al. 2021, Natur, 591, 220
Inoue, S., Aharonian, F. A., & Sugiyama, N. 2005, ApJL, 628, L9
Inoue, S., Sigl, G., Miniati, F., & Armengaud, E. 2007, arXiv:astro-ph/0701167
Inoue, S., & Takahara, F. 1996, ApJ, 463, 555
Jenkins, A., Frenk, C. S., White, S. D. M., et al. 2001, MNRAS, 321, 372
Johnson, A. R., Rudnick, L., Jones, T. W., Mendygral, P. J., & Dolag, K. 2020, ApJ, 888, 101
Jones, F. C. 1968, PhRv, 167, 1159
Kale, R., Venturi, T., Giacintucci, S., et al. 2013, A&A, 557, A99
Kamae, T., Karlsson, N., Mizuno, T., Abe, T., & Koi, T. 2006, ApJ, 647, 692
Kamae, T., Karlsson, N., Mizuno, T., Abe, T., & Koi, T. 2007, ApJ, 662, 779
Kang, H., Rachen, J. P., & Biermann, P. L. 1997, MNRAS, 286, 257
Kang, H., Ryu, D., & Ha, J.-H. 2019, ApJ, 876, 79
Kang, H., Ryu, D., & Jones, T. W. 2012, ApJ, 756, 97
Kashiyama, K., & Meszaros, P. 2014, ApJL, 790, L14
Kelner, S. R., Aharonian, F. A., & Bugayov, V. V. 2006, PhRvD, 74, 034018
Keshet, U. 2010, arXiv:1011.0729
Keshet, U., & Reiss, I. 2017, in Proc. 7th Int. Fermi Symp., 115
Keshet, U., & Loeb, A. 2010, ApJ, 722, 737
Khatri, R., & Gaspari, M. 2016, MNRAS, 463, 655
Kotera, K., Allard, D., Murase, K., et al. 2009, ApJ, 707, 370
Kushnir, D., & Waxman, E. 2009, JCAP, 2009, 002
Kushnir, D., & Waxman, E. 2010, JCAP, 2010, 025

Lisanti, M., Mishra-Sharma, S., Necib, L., & Safdi, B. R. 2016, ApJ, 832, 117
Loeb, A., & Waxman, E. 2006, JCAP, 2006, 003
McEnery, J., van der Horst, A., Dominguez, A., et al. 2019, BAAS, 51, 245
Mori, K., Tsuru, T. G., Nakazawa, K., et al. 2016, Proc. SPIE, 9905, 99051O
Moskalenko, I. V., & Strong, A. W. 1998, ApJ, 493, 694
Murase, K. 2017, in Active Galactic Nuclei as High-Energy Neutrino Sources, ed. T. Gaisser & A. Karle (Singapore: World Scientific)
Murase, K., Ahlers, M., & Lacki, B. C. 2013, PhRvD, 88, 121301
Murase, K., & Beacom, J. F. 2013, JCAP, 02, 028
Murase, K., Beacom, J. F., & Takami, H. 2012, JCAP, 2012, 030
Murase, K., Inoue, S., & Asano, K. 2009, IJMPD, 18, 1609
Murase, K., Inoue, S., & Nagataki, S. 2008, ApJL, 689, L105
Murase, K., & Waxman, E. 2016, PhRvD, 94, 103006
Nakazawa, K., Mori, K., Tsuru, T. G., et al. 2018, Proc. SPIE, 10699, 106992D
Nelson, K., Lau, E. T., & Nagai, D. 2014, ApJ, 792, 25
Ohno, H., Takizawa, M., & Shibata, S. 2002, ApJ, 577, 658
Petrosian, V., & Kang, B. 2015, ApJ, 813, 5
Pfrommer, C. 2008, MNRAS, 385, 1242
Pfrommer, C., Enßlin, T. A., & Springel, V. 2008, MNRAS, 385, 1211
Pinzke, A., Oh, S. P., & Pfrommer, C. 2017, MNRAS, 465, 4800
Pizzo, R. F. 2010, PhD thesis, Univ. Groningen
Reiprich, T. H., & Bohringer, H. 2002, ApJ, 567, 716
Riquelme, M. A., & Spitkovsky, A. 2011, ApJ, 733, 63
Rybicki, G. B., & Lightman, A. P. 1985, Radiative Processes in Astrophysics (New York, NY: Wiley)
Ryu, D., Kang, H., & Ha, J.-H. 2019, ApJ, 883, 60
Sarazin, C. L. 1999, ApJ, 520, 529
Schlickeiser, R. 2002, Cosmic Ray Astrophysics (Berlin: Springer)
Schlickeiser, R., Sievers, A., & Thiemann, H. 1987, A&A, 182, 21
Senno, N., Mészáros, P., Murase, K., Baerwald, P., & Rees, M. J. 2015, ApJ, 806, 24
Stecker, F. W. 1970, Ap&SS, 6, 377
Strong, A. W., Moskalenko, I. V., & Ptuskin, V. S. 2007, ARNPS, 57, 285
Tamborra, I., Ando, S., & Murase, K. 2014, JCAP, 2014, 043
Teraki, Y., & Asano, K. 2019, ApJ, 877, 71
Tomsick, J., Zoglauer, A., Sleator, C., et al. 2019, BAAS, 51, 98
van Weeren, R. J., de Gasperin, F., Akamatsu, H., et al. 2019, SSRv, 215, 16
Vazza, F., Angelinelli, M., Jones, T. W., et al. 2018, MNRAS, 481, L120
Venturi, T., Giacintucci, S., Brunetti, G., et al. 2007, A&A, 463, 937
Waxman, E., & Bahcall, J. 1999, PhRvD, 59, 023002
Wiener, J., Oh, S. P., & Guo, F. 2013, MNRAS, 434, 2209
Wik, D. R., Sarazin, C. L., Finoguenov, A., et al. 2011, ApJ, 727, 119
Xi, S.-Q., Wang, X.-Y., Liang, Y.-F., et al. 2018, PhRvD, 98, 063006
Yan, H., & Lazarian, A. 2002, PhRvL, 89, 281102
Yoshida, S., & Murase, K. 2020, PhRvD, 102, 083023
Yuan, C., Mészáros, P., Murase, K., & Jeong, D. 2018, ApJ, 857, 50
Zandanel, F., Pfrommer, C., & Prada, F. 2014, MNRAS, 438, 124
Zandanel, F., Tamborra, I., Gabici, S., & Ando, S. 2015, A&A, 578, A32